

POLITECNICO DI TORINO

Master's degree course in Aerospace Engineering

Master's Thesis

**Shape sensing of thin-walled structures:  
optimization of the inverse Finite  
Element Method**



**Supervisors**

Prof. Marco Gherlone

Dott. Marco Esposito

**Candidate**

Giulia Gastaldo

ACADEMIC YEAR 2019-2020



# Abstract

Structural health monitoring systems play a fundamental role in the maintenance of the vehicles integrity, thus providing a real-time monitoring of structures using shape sensing techniques. To this purpose, the inverse Finite Element Method (iFEM) is one of the most promising applied approaches. Using the local strain data obtained from in-situ sensors, iFEM is able to reconstruct the global displacement field of the examined structure.

In this thesis, the influence on iFEM accuracy due to the employment of different interpolation schemes and computing methods will be evaluated. Moreover, the applicability of the inverse FEM and of related procedures will be assessed using simplified cases derived from common aerospace structures and subsequently, its efficiency will be evaluated comparing the obtained displacements to the ones generated from correspondent direct FEM analyses.

# Contents

<b>List of Figures</b>	III
<b>1 Introduction</b>	1
<b>2 Shape sensing</b>	3
2.1 The Inverse Finite Element Method . . . . .	6
2.2 Inverse finite element formulation for shells . . . . .	7
2.3 iFEM incremental algorithm for nonlinear deformations . . . . .	13
<b>3 Gaussian Integration</b>	15
3.1 One-dimensional Integration . . . . .	16
3.2 Two-dimensional Integration . . . . .	17
3.3 Strain attribution in the iFEM method . . . . .	18
<b>4 iFEM analysis of plates</b>	21
4.1 iFEM modelling of plates . . . . .	22
4.2 iFEM and resultant errors . . . . .	29
4.3 Method 3 implementation and final results . . . . .	32
<b>5 iFEM analysis of a spar</b>	39
5.1 Geometry and properties . . . . .	39
5.2 Strain interpolation . . . . .	44
5.3 Analysis and results . . . . .	45
<b>6 Conclusions</b>	51

# List of Figures

2.1	(a) iQS4 depicted within global $(X, Y, Z)$ and local $(x, y, z)$ coordinate systems; (b) nodal degrees-of-freedom corresponding to the local frame of reference [9] . . . . .	7
2.2	(a) Mid-plane reference surface and nodal coordinates of iQS4 element (b) element in isoparametric coordinates [9] . . . . .	8
2.3	Sensor position [16] . . . . .	10
3.1	One-dimensional elements: Gauss points . . . . .	16
3.2	Gauss integration: two-dimensional element . . . . .	17
3.3	Quadrilateral element with nine integration points . . . . .	18
4.1	Plate A: mesh for direct FEM analysis . . . . .	22
4.2	Plate B: mesh for direct FEM analysis . . . . .	22
4.3	Plate A: Structural response for direct FEM analysis . . . . .	23
4.4	Plate B: Structural response for direct FEM analysis . . . . .	23
4.5	Plate A: Inverse FEM discretisation - 4x2 elements . . . . .	24
4.6	Plate B: Inverse FEM discretisation - 8x1 elements . . . . .	24
4.7	Plate A: $\epsilon_x$ . . . . .	25
4.8	Plate A: $\epsilon_y$ . . . . .	25
4.9	Plate A: $\gamma_{xy}$ . . . . .	26
4.10	Plate B: $\epsilon_x$ . . . . .	26
4.11	Plate B: $\epsilon_y$ . . . . .	27
4.12	Plate B: $\gamma_{xy}$ . . . . .	27
4.13	Plate A: Inverse FEM discretisation - 8x4 elements . . . . .	29
4.14	Plate A: Inverse FEM discretisation - 16x8 elements . . . . .	30
4.15	Plate B: Inverse FEM discretisation - 16x2 elements . . . . .	30
4.16	Plate B: Inverse FEM discretisation - 32x4 elements . . . . .	31
4.17	Plate A: $\epsilon_x$ distribution and values at sensors location - 4x2 elements . . .	35
4.18	Plate A: $\epsilon_y$ distribution and values at sensors location - 4x2 elements . . .	35
4.19	Plate A: $\gamma_{xy}$ distribution and values at sensors location - 4x2 elements . .	36

4.20	Plate B: $\epsilon_x$ distribution and values at sensors location - 8x1 elements . . .	36
4.21	Plate B: $\epsilon_y$ distribution and values at sensors location - 8x1 elements . . .	37
4.22	Plate B: $\gamma_{xy}$ distribution and values at sensors location - 8x1 elements . . .	37
5.1	Geometry . . . . .	40
5.2	Spar discretisation . . . . .	42
5.3	Details of the irregular mesh . . . . .	43
5.4	Structural response for direct FEM analysis . . . . .	43
5.5	Inverse discretisation . . . . .	44
5.6	Nodes for errors computation . . . . .	45
5.7	Spar displacement: x component . . . . .	46
5.8	Nodes for errors computation . . . . .	47
5.9	Spar displacement: x component . . . . .	48
5.10	Spar response . . . . .	49



# Chapter 1

## Introduction

The maintenance and monitoring of aerospace vehicles have become increasingly important issues for future applications. An efficient on-board structural health management system, which provides real-time monitoring of the system global state, could mitigate accidents due to structural failures. In fact, the knowledge of the real structural health condition of a structure can allow a more accurate failure prediction and the maintenance to be performed based on actual data. As a consequence, such technologies could reduce maintenance costs and inspections frequency [16]. These aspects play a fundamental role when applied loads are difficult to determine or measure, as for aerodynamic forces, vibrating excitations transmitted through junctions or impact loads [4]. The aforementioned issues are also important in the study of smart structures, such as those with morphing capabilities or structures with embedded antenna arrays that need feedback for actuation and control systems [1], [8]. Moreover, the monitoring of the deformed shape is a vital aspect for control of large deployable frame structures that carry antennas [2],[12].

For practical use, Structural Health Monitoring (SHM) systems are adopted. The monitoring occurs by means of in-situ sensors arrays which are able to detect the local strain informations. Measured data are then processed, solving an inverse problem known as shape sensing, thus obtaining a real-time reconstruction of full-field structural displacements. Shape sensing algorithm should consequently be computationally fast and robust. In this regard, one of the most promising and reliable methods to solve this problem is the inverse Finite Element Method (iFEM), which is a variational approaches that minimizes the error functional over the entire problem domain, obtained by comparing the estimated and measured strains in the least-square sense [16].

The purpose of this work is to investigate inverse FEM accuracy when different interpolation schemes and computing methods are employed. The applicability of this method will be assessed using simplified aerospace structures and, subsequently, its

efficiency will be evaluated comparing the obtained displacements to the ones generated from correspondent direct FEM analyses. Moreover, for numerical examples, different methods of strain attributions to each inverse element are to be investigated.

Chapter 2 introduces inverse finite element formulation for plates and its practical application to structures, which is the main subject of this work.

Chapter 3 is a brief introduction to the gaussian integration, as it will be useful for a deeper understanding of the procedures adopted in this study.

Chapter 4 analyses two different plates, subject respectively to transverse and shear loadings with the inverse method. The results are compared to the ones obtained from direct studies, which are used as benchmarks. Each method of strain data attribution to the Gauss points is applied to the structures and the positive and negative aspects are evaluated.

Chapter 5 takes into account an existing spar structure, and the results from the previous chapter are applied. Once again, inverse FEM errors are computed.

Chapter 6 provides some closing remarks and suggests some future developments of this subject.

## Chapter 2

# Shape sensing

Innovative technologies for maintenance and control of aerospace vehicles are developed thanks to efficient structural health monitoring (SHM) systems, which provide real-time monitoring of the vehicle's global or local structural state. Such actual knowledge of the structural health condition of a structure allows a more accurate failure prediction and the maintenance to be performed based on actual information. As a consequence, this technology could improve structural safety, reduce inspections, thus reducing costs of maintenance operations.

A SHM system uses strain sensors embedded on the structure surface. Hence, the structural deformations are obtained using real-time sensor measurements through the solution of an inverse problem known as *shape sensing*. Shape-sensing methods can be classified according to the approach used [4]:

- Numerical integration of experimental strains. Most of these methods deal with beam problem.
- Use of global continuous basis functions to approximate the displacement field. This approach uses an a priori set of functions and unknown coefficients to fit discretely measured strains.
- Use of neural network. A significant drawback of the methods based on this theory is that their accuracy depends on the choice of the training load cases.
- Application of variational approaches. In these methods, an error functional is defined and therefore minimized over the problem domain, comparing the estimated strains and their measured values obtained from the in-situ sensors.

## Numerical integration of experimental strains

Most of the methods which require the integration of in-situ measured strains deal with beam problems and have the classical beam equations as structural framework [1]. The most promising approach is the Ko's Displacement Theory [11], which is suitable to describe the structural behaviour of beams, plates and wing-boxes. The reconstruction of the deformed shape of a beam structure is obtained from double integration of measured axial strains. The sensors which provide experimental strains are located on a sensing line, at a known distance from the neutral axis. For pure bending and slender structures, Bernoulli-Euler hypotheses are assumed. Additional deflections due to transverse shear can be assessed by knowing the shear force distribution along the axis. As for bending deflection, the method is able to reconstruct the cross-section twist angle due to torsion orienting the sensors along the  $45^\circ$  direction (where  $0^\circ$  direction is considered the one along the axis of the structure). Load cases with combined effect from bending and torsion can be considered.

## Global continuous basis function

These methods employ a set of spatial functions and unknown weighting coefficients, which are used to fit the strain values obtained by sensors; the unknowns are determined by discrete measurements of the deformations [4]. The displacements are computed using strain-displacement relationships, and to this purpose the problem boundary conditions are considered. The chosen assumptions to define these strain-displacement relationships are usually the Bernoulli-Euler ones for beams and the Kirchhoff ones for plates. The basis functions which approximate the strain field can be global or piecewise continuous ([6], [7], [10]). When global basis functions are used, the number of strain measurements can be equal or larger than the number of unknown coefficients and basis functions, whereas when the piecewise ones are employed, the number of necessary measurements is larger [18].

## Neural Network

The reconstruction of the deflection is performed using different types of Neural Network. However, a significant drawback of the methods based on this theory is that their accuracy depends on the choice of the training load cases ([3],[12]).

## Variational approaches

The variational methods are the most efficient for many large-scale practical applications. Among them, one of the most promising applied approach is the inverse Finite Element Method (iFEM), firstly introduced by Tessler and Spangler [13] - [15]. This approach discretizes the problem domain using  $C^0$  (continuous) finite elements and it is based on a weighted least-squares variational formulation. IFEM can reconstruct both static and dynamic responses and it is also suitable to model complex geometries.

When iFEM was introduced, it was possible to solve problem related to small deformation, which is the field of linear load-displacement response. The existing formulation has employed the assumption of small displacements. Thus, using these methods to solve large-displacement problems lead to significant errors in the evaluation of the deformed shape.

The solution of problems concerning geometric nonlinearity requires a modification of the standard linear iFEM. The linear method is thus used over a certain number of load steps and the incremental variation of deformation is summed to determine the final deformed shape of the structure. This procedure is similar to the one used in the nonlinear Finite Element Method, which also employs a series of linear displacement increments to properly recreate the nonlinear load-deflection curve.

Shape-sensing techniques have a wide range of applications for future aircrafts and spacecrafts. Many aircraft components, such as the fuselage skin or certain wing units, are subject to compressive loading. A health monitoring system able to reconstruct the nonlinear structural response should predict the onset of buckling and the related failure. It can also be employed to study shape morphing structures in aircraft and membrane space structures, which are subject to large deformations. It is possible to use the predicted deformed shape as feedback for the actuation system for an efficient structural control.

## 2.1 The Inverse Finite Element Method

Consider the structural domain  $\Omega$ , discretized using one-, two- or three-dimensional finite elements. Adopting a Cartesian coordinate system  $\mathbf{x} \equiv (x, y, z)$ , the vector  $(u_x(\mathbf{x}), u_y(\mathbf{x}), u_z(\mathbf{x}))$  can be expressed in terms of the set of kinematic variables  $\mathbf{u}(\mathbf{x})$ . Moreover, it defines completely the displacement field experienced by the structure. Within each finite element, the kinematic variables are interpolated by a set of element shape functions

$$\mathbf{u}(\mathbf{x}) \approx \mathbf{u}^e = \mathbf{N}(x)\mathbf{q}^e, \quad (2.1)$$

where  $\mathbf{N}$  is the shape-function matrix and  $\mathbf{q}^e$  the nodal degrees of freedom.

Based on the adopted structural theory, the strain field is completely defined by a set of  $K$  independent quantities known as strain measures  $\varepsilon(\mathbf{u}^e) \equiv \{\varepsilon_k\}$ ,  $k = 1 \dots K$ . These measures can be expressed in terms of the nodal degrees of freedom

$$\varepsilon(\mathbf{u}^e) = \mathbf{B}(x)\mathbf{q}^e, \quad (2.2)$$

where  $\mathbf{B}$  is the matrix containing shape function derivatives.

Minimizing a functional defined as the least-squares error between the analytic strain measures  $\varepsilon(\mathbf{u}^e)$  and the corresponding experimental strains,  $\varepsilon^\varepsilon(\mathbf{u}^e) \equiv \{\varepsilon_k^\varepsilon\}$   $k = 1 \dots K$ , it is possible to obtain the iFEM displacement solution. The experimental strains are measured at  $n$  discrete location by strain gauges, rosettes or other types of strain sensors.

For a single element the error functional  $\Phi^e$  is given by the weighted sum of the least square component,  $\Phi_k^e$ , referred to the  $k$ -th strain measure:

$$\Phi^e(\mathbf{u}^e) = \sum_k \mathbf{w}_k^e \Phi_k^e, \quad (2.3)$$

where  $\mathbf{w}_k^e$  is the weighting coefficient and  $\Phi_k^e$  is defined as

$$\Phi_k^e = \frac{1}{n} \sum_{i=1}^n \left[ \varepsilon_{k(i)} - \varepsilon_{k(i)}^\varepsilon \right]^2, \quad k = 1 \dots K. \quad (2.4)$$

The weighting coefficients  $\mathbf{w}_k^e$  are obtained by multiplying dimensional parameters and dimensionless coefficients,  $\lambda_k^e$ . The first ones assure that the terms in the former equation have the same mathematical units, while either high or low values are assigned to  $\lambda_k^e$  coefficients to define a stronger or weaker correlation between the analytic strain values and the experimental measures.

The element functional  $\Phi^e$  is minimized with respect to the nodal unknown vector

degrees-of-freedom  $\mathbf{q}^e$ , leading to the element matrix equation  $\mathbf{a}^e \mathbf{q}^e = \mathbf{b}^e$ . Using appropriate coordinates transformation and considering problem-dependent boundary conditions, we obtain the global system of equations

$$\mathbf{A}\mathbf{q} = \mathbf{b}, \quad (2.5)$$

Where the matrix  $\mathbf{A}$  depends on the shape functions and strain sensor locations and the vector  $\mathbf{b}$  is a function of the experimental strain measures. Thus, after enforcing problem-dependent displacement boundary conditions that prevent rigid body motion, the unknown nodal degrees-of-freedom are computed by inverting the matrix  $\mathbf{A}$ . In case of small displacements, the strain-sensor locations are assumed to remain unchanged, and  $\mathbf{A}$  is inverted only once, while  $\mathbf{b}$  needs to be updated at each strain-data acquisition increment.

Since only strain-displacement relations are needed in the definition of  $\Phi^e$ , this method does not require any material properties or any information concerning the applied load. Therefore, it is suitable for both static and dynamic conditions.

## 2.2 Inverse finite element formulation for shells

The four-node inverse shell element, iQS4, has been developed based on iFEM formulation developed by Kefal et al. [9]. This element includes hierarchical drilling rotation degrees-of-freedom, thus having six DOF per node. Due to that, in the study of complex structures singular solutions can be avoided. Moreover, this inverse shell element has less tendency toward shear locking.

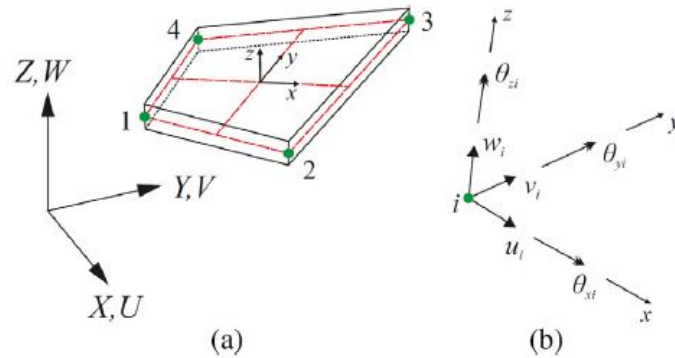


Figure 2.1: (a) iQS4 depicted within global  $(X, Y, Z)$  and local  $(x, y, z)$  coordinate systems; (b) nodal degrees-of-freedom corresponding to the local frame of reference [9]

The iQS4 formulation is obtained from a weighted-least-squares functional which has Mindlin theory as its kinematic framework. A schematic of iQS4 is shown in figure 2.1.

Consider a shell of thickness  $2t$ , for which the Cartesian coordinate system  $(x, y, z)$  sets the element frame of reference. Its origin is located at the mid-plane centroid. The  $(x, y)$  reference plane can be solely defined using bilinear isoparametric shape functions  $N_i(s, t)$ , where  $s$  and  $t$  are dimensionless isoparametric coordinates, and the element local nodal coordinates  $(x_i, y_i) \quad i = 1 \dots 4$ . Hence, the mapping functions are as follows:

$$x(s, t) \equiv x = \sum_{i=1}^4 N_i x_i \quad (2.6)$$

$$y(s, t) \equiv y = \sum_{i=1}^4 N_i y_i \quad (2.7)$$

In figure 2.2 the shift from  $(x, y)$  reference frame to isoparametric coordinates is shown.

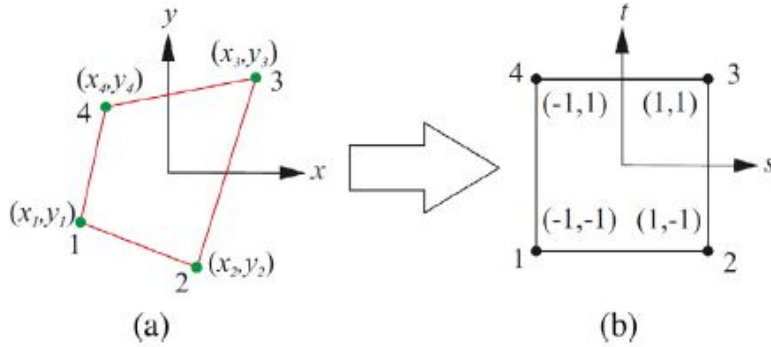


Figure 2.2: (a) Mid-plane reference surface and nodal coordinates of iQS4 element (b) element in isoparametric coordinates [9]

The  $u$  and  $v$  membrane displacement can be defined in terms of nodal DOFs:

$$u(x, y) \equiv u = \sum_{i=1}^4 N_i u_i + \sum_{i=1}^4 L_i \theta_{zi}, \quad (2.8)$$

$$v(x, y) \equiv v = \sum_{i=1}^4 N_i v_i + \sum_{i=1}^4 M_i \theta_{zi}, \quad (2.9)$$

Where  $L_i$  and  $M_i$  are the shape functions that define the interaction between the drilling rotation  $\theta_{zi}$  and the membrane displacement  $u_i$  and  $v_i$ .

The transverse displacement  $w$  and two bending rotations  $\theta_x$  and  $\theta_y$  are defined as

$$w(x, y) \equiv w = \sum_{i=1}^4 N_i w_i - \sum_{i=1}^4 L_i \theta_{xi} - \sum_{i=1}^4 M_i \theta_{yi} \quad (2.10)$$

$$\theta_x(x, y) \equiv \theta_x = \sum_{i=1}^4 N_i \theta_{xi} \quad (2.11)$$

$$\theta_y(x, y) \equiv \theta_y = \sum_{i=1}^4 N_i \theta_{yi} \quad (2.12)$$

Where  $w$  is the average transverse deflection,  $\theta_x$  and  $\theta_y$  are the positive counter clockwise rotations around the  $x$  and  $y$  axes respectively. Using equations (2.8) - (2.12), the components of displacement vector are given according to Mindlin plate theory, as

$$u_x(x, y, z) \equiv u_x = u + z\theta_y, \quad (2.13)$$

$$u_y(x, y, z) \equiv u_y = v - z\theta_x, \quad (2.14)$$

$$u_z(x, y, z) \equiv u_z = w, \quad (2.15)$$

where  $u_x$ ,  $u_y$  are in-plane displacements and  $u_z$  is the transverse deflection across the uniform shell thickness. The strain-displacement relations of linear elasticity are

$$\varepsilon_{xx} = \frac{\partial u_x}{\partial x} = \frac{\partial u}{\partial x} + z \frac{\partial \theta_y}{\partial x} \quad (2.16)$$

$$\varepsilon_{yy} = \frac{\partial u_y}{\partial y} = \frac{\partial v}{\partial y} - z \frac{\partial \theta_x}{\partial y} \quad (2.17)$$

$$\gamma_{xy} = \frac{\partial u_x}{\partial y} + \frac{\partial u_y}{\partial x} = \frac{\partial v}{\partial x} + \frac{\partial u}{\partial y} + z \left( \frac{\partial \theta_y}{\partial y} - \frac{\partial \theta_x}{\partial x} \right) \quad (2.18)$$

$$\gamma_{xz} = \frac{\partial u_z}{\partial x} + \frac{\partial u_x}{\partial z} = \frac{\partial w}{\partial x} + \theta_y \quad (2.19)$$

$$\gamma_{yz} = \frac{\partial u_z}{\partial y} + \frac{\partial u_y}{\partial z} = \frac{\partial w}{\partial y} - \theta_x \quad (2.20)$$

The theory assumption of  $\sigma_{zz} = 0$  implies that the transverse-normal strain  $\varepsilon_{zz}$  does not contribute to the strain energy. It is now possible to identify within these strain

measures three membrane, three bending strains and two transverse shears:

$$\mathbf{e} = \{u_{,x} , v_{,y} , u_{,y} + v_{,x}\}^T \quad (2.21)$$

$$\mathbf{k} = \{\theta_{y,x} , \theta_{x,y} , \theta_{y,y} - \theta_{x,x}\}^T \quad (2.22)$$

$$\mathbf{g} = \{w_{,x} + \theta_x , w_{,y} + \theta_y\}^T \quad (2.23)$$

Combining equations (2.16)-(2.20) into equations (2.21)-(2.23), the strain-displacement relations may be expressed in terms of element nodal degrees-of-freedom:

$$\begin{Bmatrix} \varepsilon_{xx} \\ \varepsilon_{yy} \\ \gamma_{xy} \end{Bmatrix} = \mathbf{e} + z\mathbf{k} = \mathbf{B}^m \mathbf{q}^e + z\mathbf{B}^b \mathbf{q}^e \quad (2.24)$$

$$\begin{Bmatrix} \gamma_{xz} \\ \gamma_{yz} \end{Bmatrix} = \mathbf{g} = \mathbf{B}^s \mathbf{q}^e \quad (2.25)$$

The experimental membrane and bending curvature strain measures,  $\mathbf{e}_{(i)}^\varepsilon$  and  $\mathbf{k}_{(i)}^\varepsilon$ , are obtained by in-situ sensors. These can be evaluated at the sensor location  $(x_i, y_i)$  from measurements on the top and bottom surfaces as shown in figure 2.3.

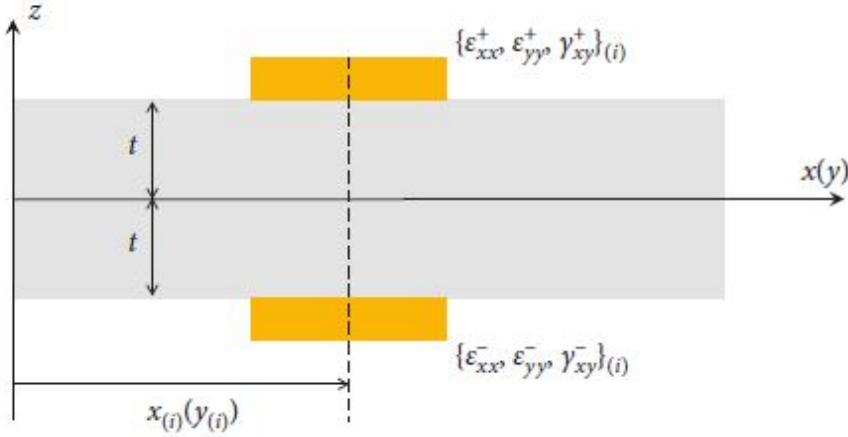


Figure 2.3: Sensor position [16]

The experimental measures are

$$\mathbf{e}_{(i)}^\varepsilon = \frac{1}{2} \left\{ \left( \varepsilon_{xx}^+ + \varepsilon_{xx}^- \right), \left( \varepsilon_{yy}^+ + \varepsilon_{yy}^- \right), \left( \gamma_{xy}^+ + \gamma_{xy}^- \right) \right\}_{(i)}^T \quad (2.26)$$

$$\mathbf{k}_{(i)}^\varepsilon = \frac{1}{2t} \left\{ \left( \varepsilon_{xx}^+ - \varepsilon_{xx}^- \right), \left( \varepsilon_{yy}^+ - \varepsilon_{yy}^- \right), \left( \gamma_{xy}^+ - \gamma_{xy}^- \right) \right\}_{(i)}^T \quad (2.27)$$

The transverse shear strains cannot be evaluated experimentally. A smoothing procedure, known as Smoothing Element Analysis (SEA), enables the first order derivatives of  $\mathbf{k}_{(i)}^\varepsilon$  to be computed; the result can be used to obtain  $\mathbf{g}_{(i)}^\varepsilon$ . However, in the deformation of thin shells the transverse shear strain contributions are much smaller compared to the bending curvatures. In this case, it is possible to omit the  $\mathbf{g}_{(i)}^\varepsilon$  contribution to the iFEM formulation. Hence, the corresponding functional is expressed as follows ( $k = 7, 8$ )

$$\Phi_k^e = \int \varepsilon_{k(i)}^2 (u^e) dA \quad (2.28)$$

The former integral is computed over the element surface  $A^e$ . Furthermore, corresponding  $\lambda_k^e$  are set to small values ( $10^{-4}$ ) related to unity, which is assigned to the other  $\lambda_k^e$  coefficients ( $k = 1, \dots, 6$ ). Similarly, in case of a missing in-situ component, the former equation is used for all strain measures and the dimensionless weighting constants  $\lambda_k^e$  are set to small values ( $10^{-4}$ ), relative to 1 which is used for the elements where sensors are available. Thus, an iFEM discretization can have sparse measured strain data, and still the necessary interpolation connectivity can be maintained between the elements that have strain-sensor data.

It is now possible to define the individual inverse element functional.  $\Phi^e(\mathbf{u}^e)$  accounts for membrane, bending and transverse shear deformation.

$$\Phi^e(\mathbf{u}^e) = \mathbf{w}_m^e \|\mathbf{e}(\mathbf{u}^e) - \mathbf{e}^\varepsilon\|^2 + \mathbf{w}_k^e \|\mathbf{k}(\mathbf{u}^e) - \mathbf{k}^\varepsilon\|^2 + \mathbf{w}_g^e \|\mathbf{g}(\mathbf{u}^e)\|^2. \quad (2.29)$$

The functional can be minimized with respect to the nodal displacement DOF:

$$\frac{\partial \Phi^e}{\partial q^e} = \mathbf{a}^e \mathbf{q}^e - \mathbf{b}^e = 0 \quad (2.30)$$

Where  $\mathbf{a}^e$  is the element left-hand-side matrix and  $\mathbf{b}^e$  a right-hand-side vector, which is function of the measured strain values. The element matrix  $\mathbf{a}^e$  can be written in terms of  $\mathbf{B}^m$ ,  $\mathbf{B}^b$  and  $\mathbf{B}^s$ , which are the derivatives of the shape functions matrix, and their corresponding weighting constants

$$\mathbf{a}^e = \int \left( w_e (\mathbf{B}^m)^T \mathbf{B}^m + w_k (2h)^2 (\mathbf{B}^b)^T \mathbf{B}^b + w_g (\mathbf{B}^s)^T \mathbf{B}^s \right) dA \quad (2.31)$$

$$\mathbf{b}^e = \frac{1}{n} \int \left( w_e (\mathbf{B}^m)^T \varepsilon_{k(i)}^\varepsilon + w_k (2h)^2 (\mathbf{B}^b)^T k \right) dA \quad (2.32)$$

Once the element local matrix equations are established, the element contributions can be assembled, giving the global linear equation system as a result. It can be obtained thanks to the following relations:

$$\mathbf{A} = \sum_{e=1}^{n_{el}} (\mathbf{T}^e)^T \mathbf{a}^e \mathbf{T}^e \quad (2.33)$$

$$\mathbf{b} = \sum_{e=1}^{n_{el}} (\mathbf{T}^e)^T \mathbf{b}^e \quad (2.34)$$

$$\mathbf{q} = \sum_{e=1}^{n_{el}} (\mathbf{T}^e)^T \mathbf{q}^e \quad (2.35)$$

$$(2.36)$$

where  $\mathbf{T}^e$  is the transformation matrix from the local to the global coordinate system,  $\mathbf{A}$  is the global left-hand-side matrix,  $\mathbf{q}$  is the global nodal displacement vector,  $\mathbf{b}$  a global right-hand-side vector and the parameter  $n_{el}$  represents the total number of inverse finite elements.

It is now possible to explicit the global system of equations (2.5)

$$\mathbf{A}\mathbf{q} = \mathbf{b}.$$

The global matrix  $\mathbf{A}$  incorporates the rigid body motion mode of the structure. Thus, it is a singular matrix. Using problem-specific boundary conditions, the former system of equations can be reduced, as

$$\mathbf{A}_R \mathbf{q}_R = \mathbf{b}_R, \quad (2.37)$$

where  $\mathbf{A}_R$  is a positive-definite matrix, therefore it is invertible. This matrix remains the same for a given distribution of strain sensors and its inverse should be computed only once during the monitoring process. On the contrary, the vector  $\mathbf{b}_R$  depends on the discrete surface strain data obtained from in-situ strain sensors. Hence, it needs to be updated during every deformation cycle.

Finally, vector  $\mathbf{q}_R$  is obtained from the matrix-vector multiplication  $\mathbf{A}_R^{-1} \mathbf{b}_R$ . This vector provides the real-time deformed structural shape. Using the evaluated displacement values, the continuous strain field of the structure can be obtained. Furthermore, it is possible to determine the stress distribution using the stress-strain constitutive relations. Lastly, a suitable failure criterion can be used for damage detection as part of the SHM process.

## 2.3 iFEM incremental algorithm for nonlinear deformations

Herein, the procedure to reconstruct nonlinear deformation will be presented. It is assumed that the adopted strain-sensor measurement system is capable of real-time measures as the structure undergoes deformation under quasistatic or dynamic loading. Using the strain increments, it is possible to employ the standard linear iFEM at each incremental load level to reconstruct the current deformed shape. The geometry shall then be updated, and the former process repeated using the next strain increment. Hence, nonlinear deformations (large displacements) are obtained in real time as the strain history becomes available from the in-situ sensors.

The procedure can be explicit as follows [16]:

- At each load level,  $i$ , the incremental section strains are evaluated experimentally or with a nonlinear direct FEM analysis.
- iFEM analysis is performed and the strain increments are used to obtain the nodal-degrees-of-freedom,  $q_i$
- The former structural geometry is then updated using the iFEM determined displacements i.e.  $x_{i+1} = x_i + N(x_i)q_i$  (where  $x$  is the iFEM nodal coordinate position).
- Based on the current geometry, the orientation of the measured strains is also updated,  $x_{i+1}$ .
- The incremental procedure is repeated until the strain history is complete.

The iFEM incremental procedure agrees with the one used for nonlinear analysis of the direct FEM, although the iFEM approach does not need to invoke equilibrium iterations at each load level. The reason of this lies in the fact that iFEM has no access to equilibrium equations. Instead, its equations smooth the measured strain data and integrate the strain-displacement relations. Since strain measures are updated at each load increment, the strain-displacement relations are constantly updated. Thus, the strain-level updates provide the necessary corrections at each load level and consequently this procedure can efficiently reconstruct highly accurate geometrically nonlinear deformations.



## Chapter 3

# Gaussian Integration

The inverse Finite Element Method, as direct FEM, requires the computation of integral matrices which are then to be analysed by the method. To overcome the difficulty of the exact computation of the aforementioned integrals, numerical methods are adopted. Numerical integration can be defined as

$$\int_a^b f(x) dx = \sum_{i=1}^n w_i f(x_i) \quad (3.1)$$

Where  $w_i$  represent the weighting coefficients,  $n$  is the number of grid points and  $x_i$  are the location of the former points. Several methods can be used, but Gaussian quadrature rules are hereafter taken into account.

Some numerical methods enable the computation of an approximate solution by forcing the polynomial to pass through a certain number of established points, which are equally spaced. These methods provide an error of  $\Delta^n$  order, where  $\Delta$  is the space between integration points. When it is possible to choose the evaluation points, the error decrease consistently. Gauss quadrature is based on the choice of special values of weights and abscissas, which are also known as Gauss points. This approach makes assumptions on both the values assumed by the function in the Gauss points and the location of these points. It is thus possible to determine a polynomial of  $2n - 1$  degree ( $2n$  unknown coefficients for  $2n$  equations) and the error will be consequently  $\Delta^{2n}$ , smaller than the one obtained from the previous methods. It is clear that the degree of polynomial increases proportionally with number of points used. To solve the system of equations complex mathematical handlings are arranged, and the final solution is obtained using Legendre polynomials. In the following paragraphs, one- and two-dimensional integrations are examined.

### 3.1 One-dimensional Integration

In Finite Element Analysis, and in the inverse FEM, numerical integration is adopted in the reference domain  $\xi \in [-1, +1]$ . Hence, all values are transformed in this configuration.

$$\int_a^b f(x) dx = \int_{-1}^1 f(\xi) \frac{dx}{d\xi} d\xi = \int_{-1}^1 f(\xi) J^e(\xi) d\xi \quad (3.2)$$

Where  $f(\xi)$  is the integrated function and  $J^e(\xi)$  is the Jacobian of the transformation derivatives from the physical to the reference coordinates.

$$J^e(\xi) = \frac{dx}{d\xi} = \sum_{i=1}^n \frac{dN_i(\xi)}{d\xi} x_i \quad (3.3)$$

$N_i$  are the shape functions and  $x_i$  the nodal coordinates.

$$\int_{-1}^1 f(\xi) \frac{dx}{d\xi} d\xi = \sum_{i=1}^n f(\xi_p) J_e(\xi_p) w_p \quad (3.4)$$

Where  $\xi_p$  are the Gauss coordinates and  $w_p$  are the weighting coefficients. In figure 3.1 different Gauss point locations are shown in figure 3.1, and in table 3.1, the correspondent  $\xi_p$  and  $w_p$  are reported.  $n_p$  is the total number of Gauss points ( $n_p = nXn$ ).

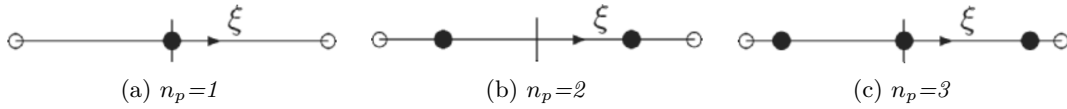


Figure 3.1: One-dimensional elements: Gauss points

Table 3.1: One-dimensional elements:  $\xi_p$  and  $w_p$

$n_p$	$p$	$\xi_p$	$w_p$
1	1	0	2
2	1	$1/\sqrt{3}$	1
	2	$1/\sqrt{3}$	1
3	1	$-\sqrt{3/5}$	5/9
	2	0	8/9
	3	$\sqrt{3/5}$	5/9

As previously mentioned, the choice of the number of grid points defines the accuracy of the adopted polynomial. Therefore, when choosing the number of Gauss points, the complexity of the approximated function must be considered.

### 3.2 Two-dimensional Integration

Quadrilateral elements are hereby considered. For the integration over the element surface  $A^e$ , it is again necessary to move from the physical plane of the element domain  $\Omega^e$  to the reference  $\xi$ - $\eta$  coordinate system in the reference element  $\Omega_\square$ .

$$\int_{\Omega_e} f(\mathbf{X}) dA = \int_{\Omega_\square} f(\boldsymbol{\xi}) \det \mathbf{J}^e(\boldsymbol{\xi}) d\Omega = \int_{-1}^1 \int_{-1}^1 f(\xi, \eta) \det \mathbf{J}^e d\xi d\eta \quad (3.5)$$

Numerical integration is again performed as follows

$$\int_{-1}^1 \int_{-1}^1 f(\xi, \eta) \det \mathbf{J}^e d\xi d\eta \approx \sum_{p=1}^{n_p} g(\zeta_p, \eta_p) \det \mathbf{J}^e(\xi_p, \eta_p) W_p \quad (3.6)$$

Where  $J^e$  is again the Jacobian of the transformation derivatives.

$$\mathbf{J}^e = \begin{bmatrix} \frac{dx}{d\xi} & \frac{dy}{d\xi} \\ \frac{dx}{d\eta} & \frac{dy}{d\eta} \end{bmatrix}$$

Once more, in figure 3.2 different Gauss point locations are shown in figure 3.2, and in table 3.2, the correspondent  $\xi_p$  and  $w_p$  are reported.

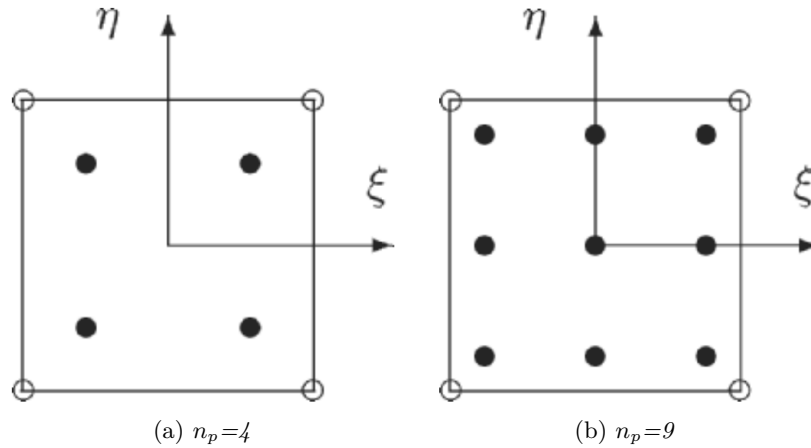


Figure 3.2: Gauss integration: two-dimensional element

As mentioned before, using  $n$  evaluation points will introduce  $2n$  unknowns ( $\xi$  and  $\eta$  at each location), and it is possible to obtain the exact integration of a polynomial of  $2n-1$  degree. Hence, using a four-points quadrilateral element ( $n=2$ ) leads to the exact integration of a third order polynomial, whereas a nine-points quadrilateral element ( $n=3$ ) exactly integrates a quintic polynomial.

Table 3.2: Two-dimensional elements:  $\xi_p$  and  $w_p$

$n_p$	$p$	$\xi_p$	$\eta_p$	$w_p$
4	1	$-1/\sqrt{3}$	$-1/\sqrt{3}$	1
	2	$1/\sqrt{3}$	$-1/\sqrt{3}$	1
	3	$-1/\sqrt{3}$	$1/\sqrt{3}$	1
	4	$1/\sqrt{3}$	$1/\sqrt{3}$	1
9	1	$-\sqrt{3/5}$	$-\sqrt{3/5}$	25/81
	2	0	$-\sqrt{3/5}$	40/81
	3	$\sqrt{3/5}$	$-\sqrt{3/5}$	25/81
	4	$-\sqrt{3/5}$	0	40/81
	5	0	0	64/81
	6	$\sqrt{3/5}$	0	40/81
	7	$-\sqrt{3/5}$	$\sqrt{3/5}$	25/81
	8	0	$\sqrt{3/5}$	40/81
	9	$\sqrt{3/5}$	$\sqrt{3/5}$	25/81

For two-dimensional finite element analysis, nine integration points are preferred as it is possible to depict accurately complex functions, thus obtaining a structural behaviour which is closer to the one actually developed by the investigated structure.

### 3.3 Strain attribution in the iFEM method

It is clear from the previous section that the values integrated over the Gauss points must be precise in order to obtain the best depiction possible of the real behaviour. In the inverse finite element method the values which need to be integrated are the strains, and they are obtained from in-situ sensors. Nine Gauss points quadrilateral element are taken into account (figure 3.3), and consequently having the exact strain data implies that nine sensors are located on each element. However, it is also possible to evaluate other cost-saving options.

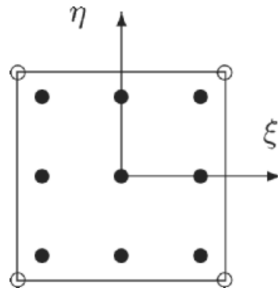


Figure 3.3: Quadrilateral element with nine integration points

Three different iFEM approaches are considered. The difference between these methods resides in the strain attributions to the nine Gauss points of the quadrilateral element.

- Method 1, in which each inverse element has only one sensor, located at the centroid. The detected strain values are assigned to all the other eight Gauss points, but there is just one exact value. Deformation is uniform over a single element.
- Method 2, in which the sensors are again located at the element centroids. The deformations are associated with a factor of 1 to the centroid (where the exact values are found) and with a factor of  $10^{-4}$  to others Gauss points.
- Method 3, the sensors are located at each Gauss point of the quadrilateral element. It is more accurate and costly than the other approaches.

In this thesis, these three approaches will be firstly applied to simple structures and the obtained results will be compared. The first two methods are already implemented in the Matlab script, whereas the third method implementation will be an output of this study.



## Chapter 4

# iFEM analysis of plates

The application of the inverse finite element method is hereafter presented using two different plates, one subjected to transverse loading and the other one to shear loading. During this study, no experimental tests are performed on the structures. Thus, direct finite element analyses are carried out to obtain the strain measurements as input data and displacements as benchmark for iFEM analyses. The precision of the iFEM prediction is then evaluated by computing the Root Mean Square (RMS) of the nodal displacement error with respect to the direct FEM results.

$$\%e_{RMS} = 100 \sqrt{\frac{1}{m} \sum_{i=1}^n \left( \frac{w_i^{\text{iFEM}} - w_i^{\text{FEM}}}{w_{\max}^{\text{FEM}}} \right)^2} \quad (4.1)$$

where  $m$  is the number of nodes in which deflection is evaluated and it is the same for both analyses.

As aforementioned, three different strain attribution approaches are considered. At first, method 1 and 2 are used. In both cases, strain sensors are located at the element centroids, where the only exact strain value is found. The first method then associates to the other Gauss points the value detected by sensors (hence we have uniform strains over each element), whereas the second one associates deformations to integration points by multiplying the centroid value for a small factor, so that these strains will be less influential in the final results. In the second section, the two approaches are compared. Finally the third method, which uses sensors located at each Gauss point location, is implemented and applied to studied structures. Again, its accuracy is compared to the ones obtained from the other methods.

## 4.1 iFEM modelling of plates

Two rectangular cantilever plates are herein studied. The dimensions of the two structures are reported in the following table.

Table 4.1: Dimensions

Plate	Length	Height	Thickness
A	1600 mm	700 mm	2 mm
B	1600 mm	200 mm	2 mm

Both plates are made of an aluminium alloy (elastic modulus  $E=73000$  MPa, Poisson's ratio  $\nu=0.3$ ). Plate A has a uniformly distributed transverse load of  $1 \frac{N}{mm^2}$ , while a uniformly distributed shear load of  $1 \frac{N}{mm^2}$  is applied to plate B.

Both structures are discretized using quadrilateral element having side 10 mm. Thus, plate A presents a mesh of 11200 elements and 11431 nodes, whereas plate B has 3200 elements and 3381 nodes. The two meshes are shown in figures 4.1 - 4.2.

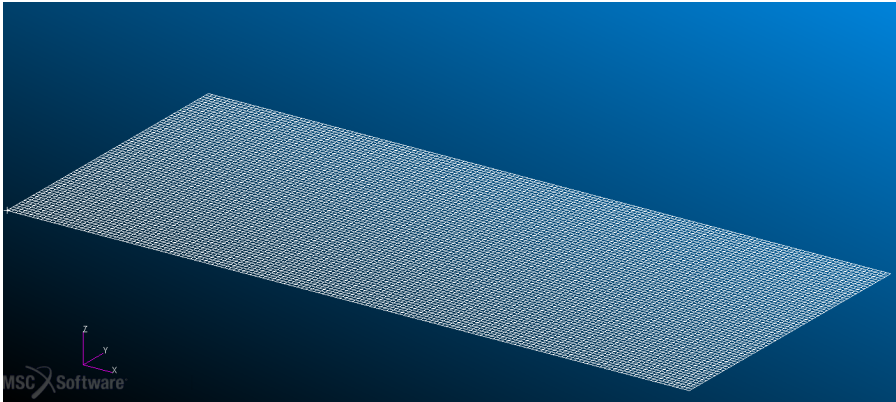


Figure 4.1: Plate A: mesh for direct FEM analysis

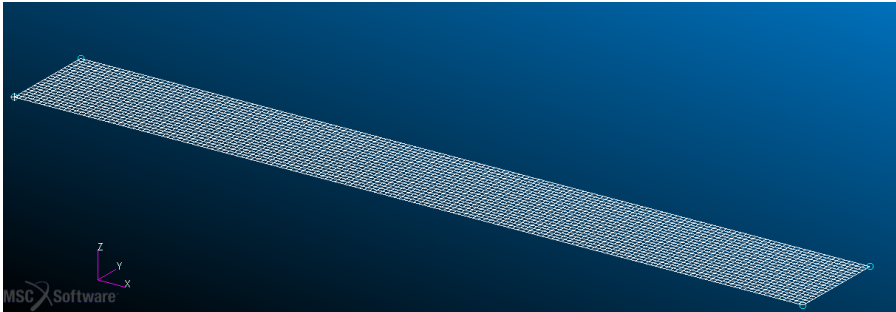


Figure 4.2: Plate B: mesh for direct FEM analysis

The structural response of both plates is analysed, as shown in figures 4.3 and 4.4. The strains are then obtained in the element centroids and the structural displacements are requested at specific node locations, thus enabling a comparison between direct and inverse FEM.

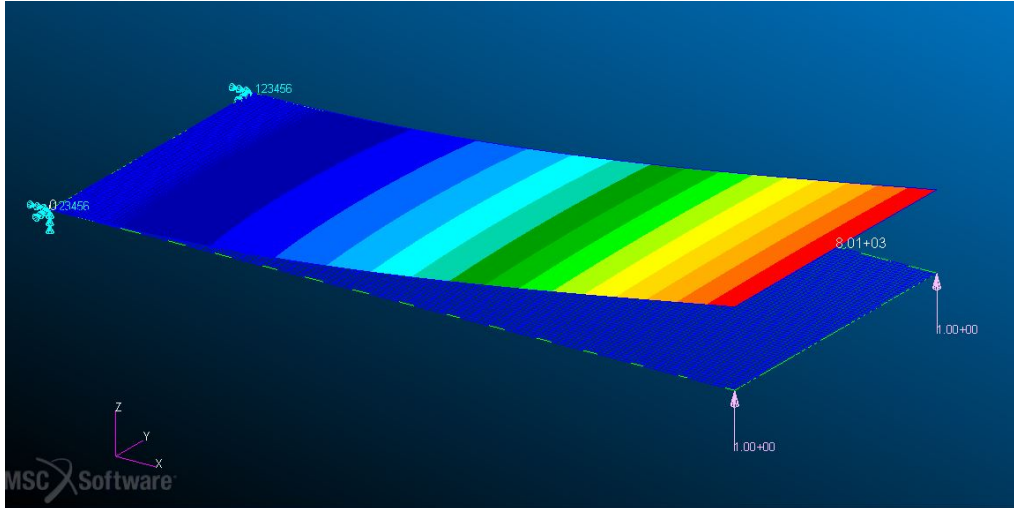


Figure 4.3: Plate A: Structural response for direct FEM analysis

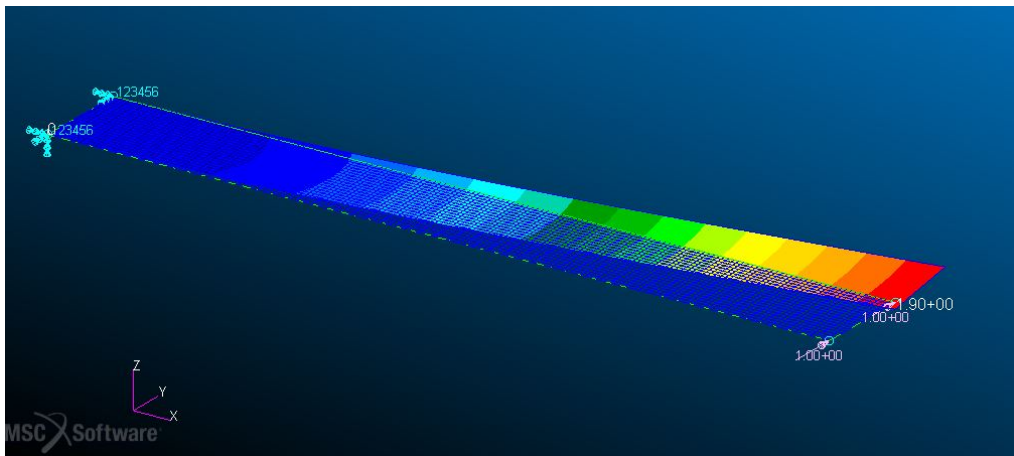


Figure 4.4: Plate B: Structural response for direct FEM analysis

It is now possible to proceed with the creation of the inverse meshes shown in figures 4.5 and 4.6, which are needed to evaluate the locations of the element centroids. In fact, the strains used as input data for the inverse analysis are obtained from the interpolation of the ones found from the direct study. The Matlab interpolating program receives as an input the  $(x, y)$  coordinates of the points where the deformation data are needed, which are as mentioned the inverse element centroids.

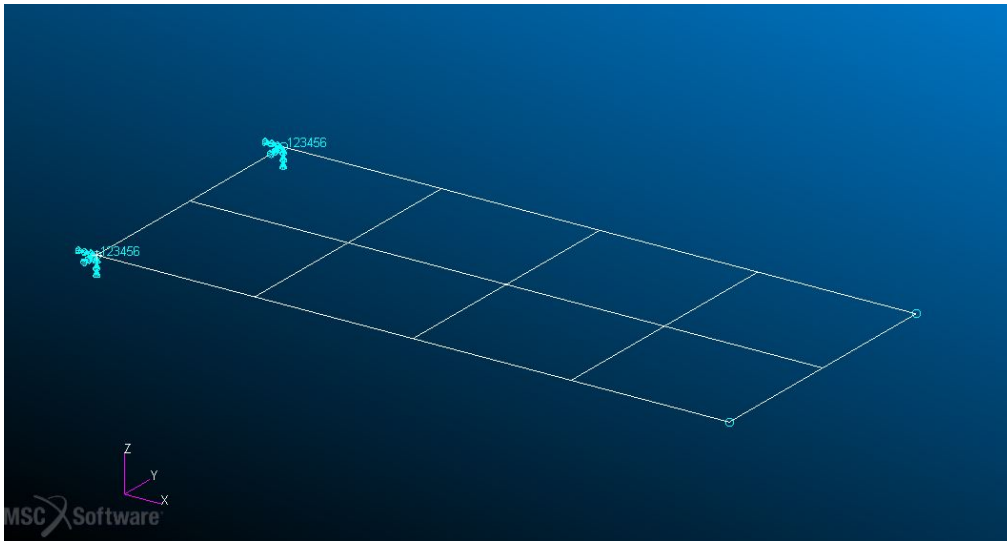


Figure 4.5: Plate A: Inverse FEM discretisation - 4x2 elements

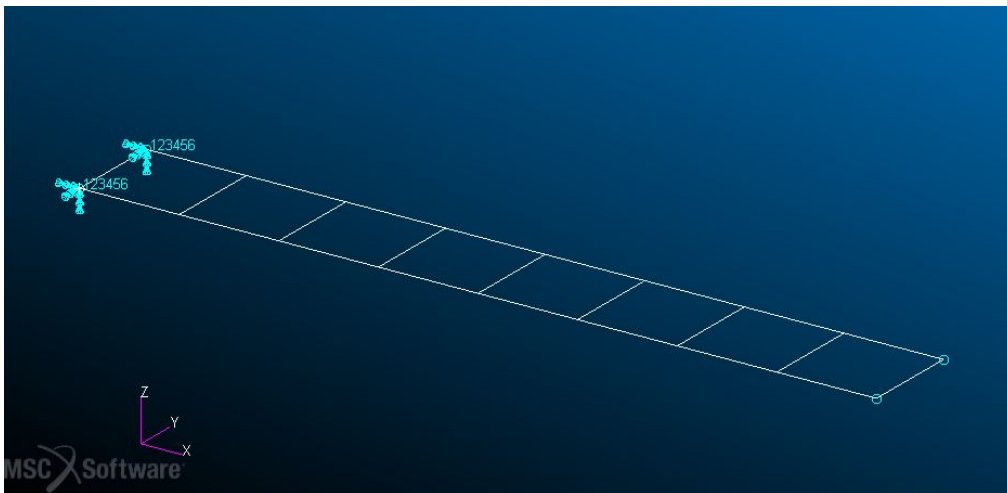


Figure 4.6: Plate B: Inverse FEM discretisation - 8x1 elements

The geometries are simple, thus a global interpolation can be performed using *interp2*. This Matlab function interpolates to find the strain values at the investigated points. Several methods of interpolation are available, the one chosen for these cases is the spline interpolation, as it results in a correct representation of the strain distributions. The vectors of  $\varepsilon_x$ ,  $\varepsilon_y$  and  $\gamma_{xy}$  are found. In figures 4.7-4.9 and 4.10-4.12 the strain distributions for plates A and B respectively are shown.

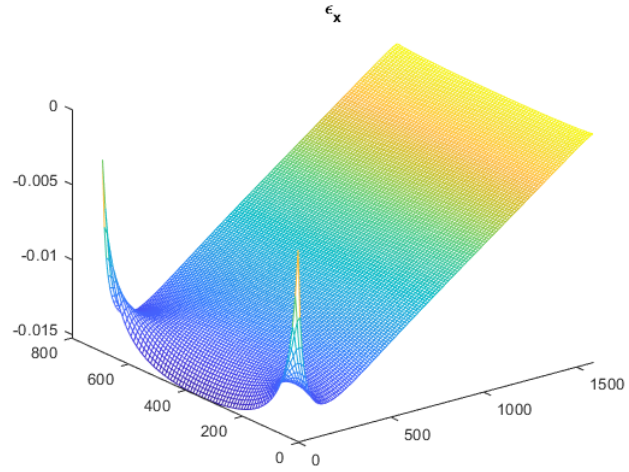


Figure 4.7: Plate A:  $\epsilon_x$

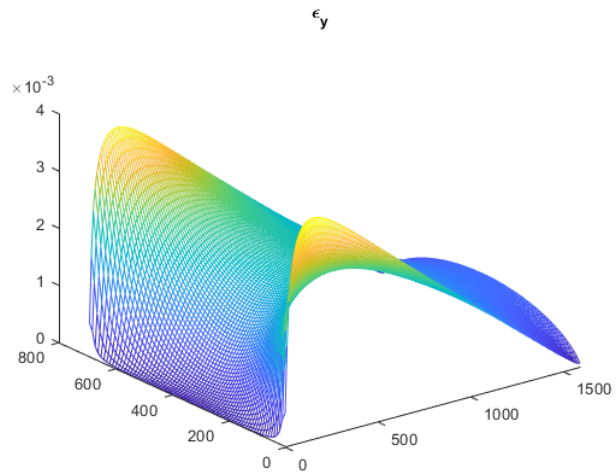


Figure 4.8: Plate A:  $\epsilon_y$

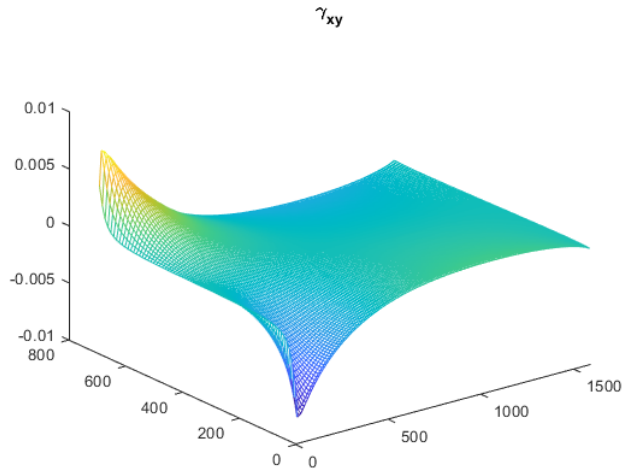


Figure 4.9: Plate A:  $\gamma_{xy}$

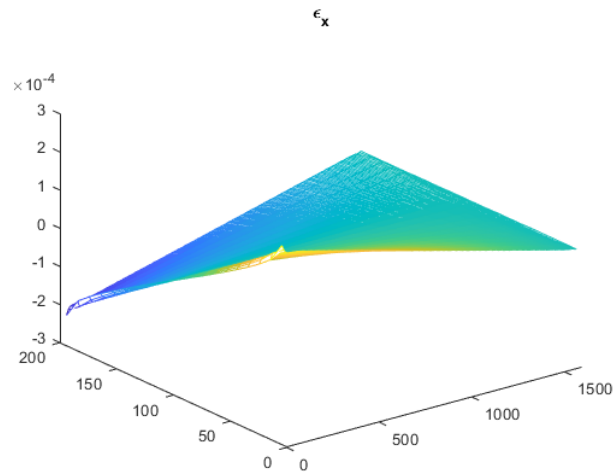


Figure 4.10: Plate B:  $\epsilon_x$

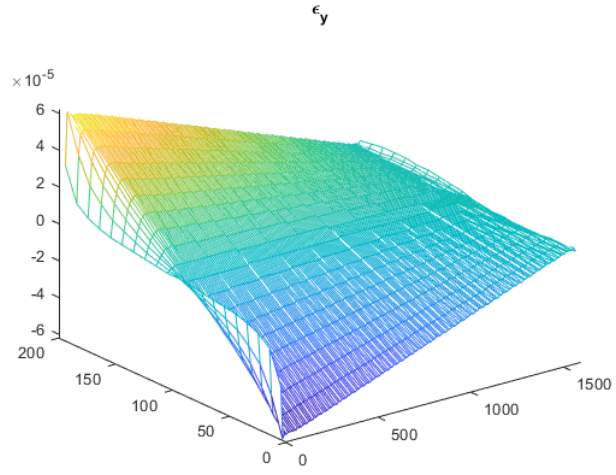


Figure 4.11: Plate B:  $\epsilon_y$

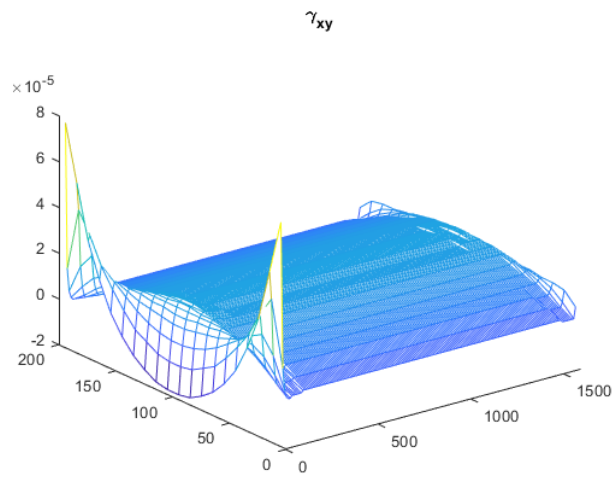


Figure 4.12: Plate B:  $\gamma_{xy}$

The initial discretizations are sparse as shown in the figures above. As mentioned in the previous paragraph, loads and materials are not necessary for the inverse study of a structure, thus they are not applied to the iFEM models. Only constraints are needed. Thus, since direct FEM meshes are dense, strain data can be accurately interpolated, and the deformations can be obtained at the desired locations of the inverse models.

The inverse finite element theory is applied to the examined plates and the resultant errors from both methods are computed, with respect to the nodal direct FEM displacements. Results are shown in tables 4.2 and 4.3, for plate A and B respectively.

Table 4.2: Plate A: RMS errors

Method	RMS_u [%]	RMS_v [%]	RMS_w [%]
1	-	-	1.25
2	-	-	1.33

Table 4.3: Plate B: RMS errors

Method	RMS_u [%]	RMS_v [%]	RMS_w [%]
1	72.70	51.00	-
2	72.70	51.00	-

As expected, the errors are present in the load directions only. The results for plate A are quite satisfactory, while for plate B errors are non-negligible and they are the same for both methods. That is probably due to the mesh sparsity, there are not enough inverse elements to describe the displacements of the structure.

## 4.2 iFEM and resultant errors

Refined meshes are hereby created for both models to verify whether the influence of the inverse discretization (and thus the increase of in-situ sensors) causes a significant decrease in errors. Hence, two different meshes are created for both cases, as shown in figures 4.13 - 4.16. Figures 4.13 and 4.15 show 32-elements inverse meshes, while figures 4.14 and 4.16 show 128-elements discretizations. The new inverse FEM analyses are carried out and the results are compared to the previous direct studies. Once again, the RMS errors are computed.

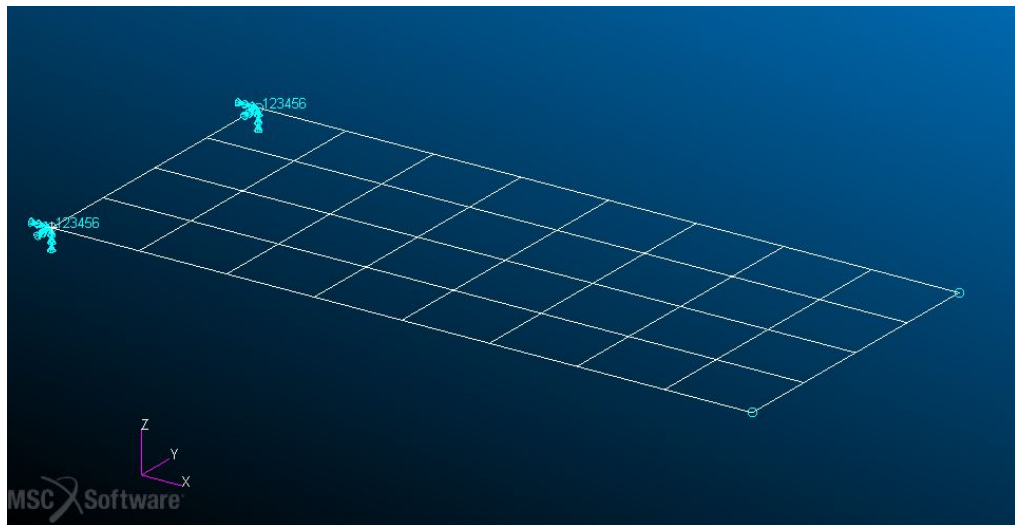


Figure 4.13: Plate A: Inverse FEM discretisation - 8x4 elements

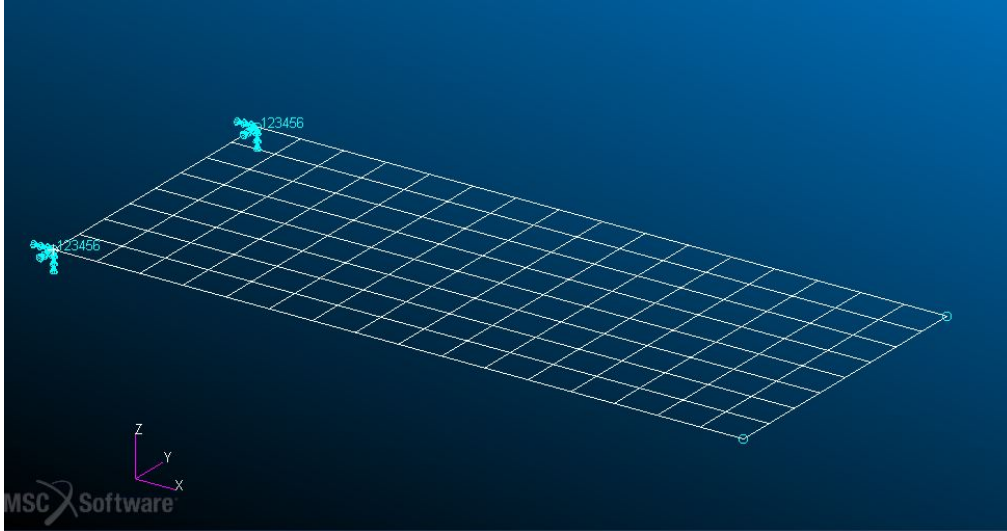


Figure 4.14: Plate A: Inverse FEM discretisation - 16x8 elements

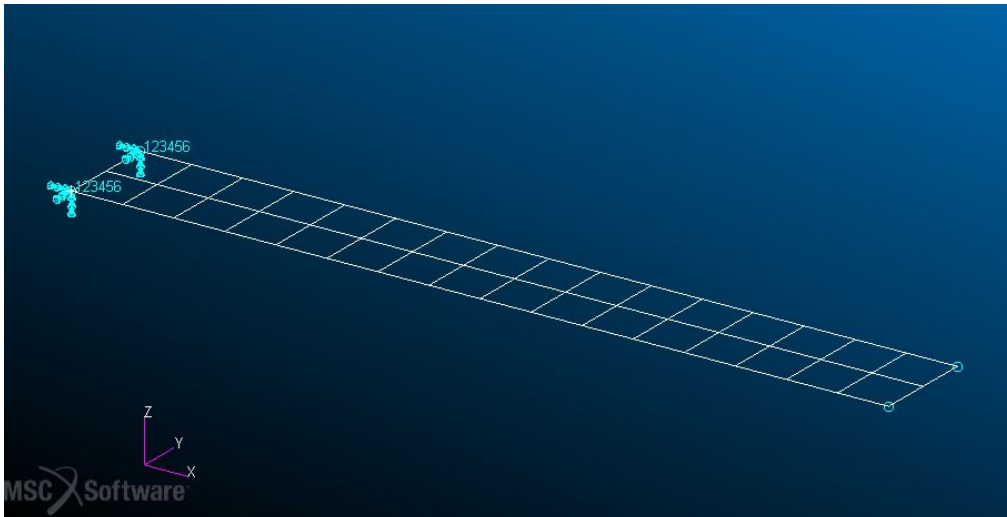


Figure 4.15: Plate B: Inverse FEM discretisation - 16x2 elements

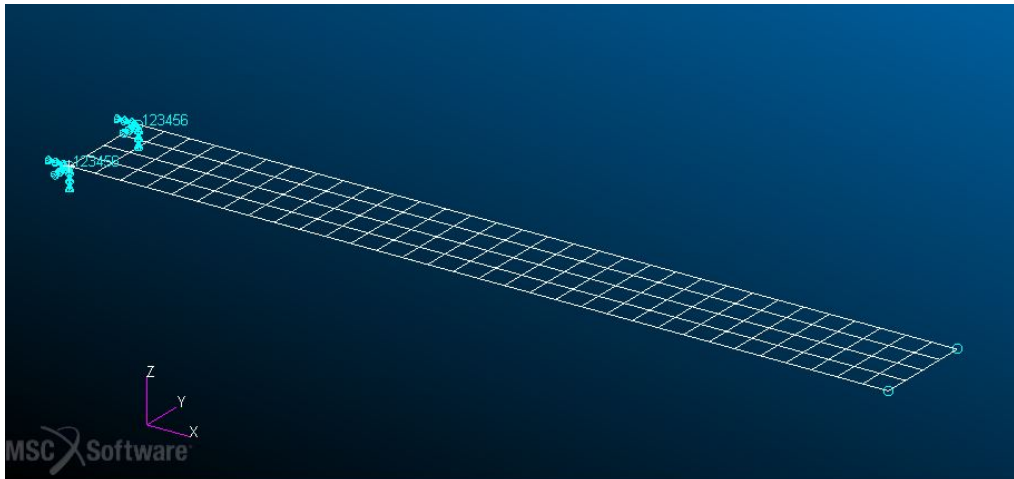


Figure 4.16: Plate B: Inverse FEM discretisation - 32x4 elements

The results presented in tables 4.4 and 4.5 show a global decrease of errors as the two meshes become more detailed. Plate A, which has low errors also in the initial discretization, has a coherent reduction of the RMS with the two refined meshes. It is possible to point out that the results from the plates having 32 elements are already accurate, therefore it is not necessary to increase the number of sensors used, as this would be more costly both economically and practically. Plate B is subject to a strong decrease of the errors, and this effect is more noticeable when the second method is used. Method 1, which is easier to employ, is nevertheless coarser. Hence, for complex strain distributions this method is not suitable, as it imposes the strain uniformity over each element. Method 2 is thus more suitable for the study of the in-plane distributed load and the 32-element plate results are already valid.

Table 4.4: Plate A: RMS errors of the refined meshes

<b>n. elements</b>	<b>Method</b>	<b>RMS_u [%]</b>	<b>RMS_v [%]</b>	<b>RMS_w [%]</b>
8x4	1	-	-	0.33
	2	-	-	0.29
16x8	1	-	-	0.082
	2	-	-	0.081

Table 4.5: Plate B: RMS errors of the refined meshes

<b>n. elements</b>	<b>Method</b>	<b>RMS_u [%]</b>	<b>RMS_v [%]</b>	<b>RMS_w [%]</b>
16x2	1	18.12	12.74	-
	2	0.11	0.08	-
32x4	1	4.48	3.11	-
	2	0.096	0.061	-

### 4.3 Method 3 implementation and final results

It is now possible to further investigate iFEM behaviour carrying out the analyses of the two plates once more. The purpose of this last study will be to implement the third method and to evaluate its effectiveness and reliability by comparing it with the other fully-developed methods. As previously mentioned, in this approach sensors are located at each integration points, thus requiring a considerable amount of sensors, one for each Gauss point of the quadrilateral element. It is believed to be more accurate than methods 1 and 2 but it presents further complications concerning higher costs of the experimental

trial and greater complexity of sensors installation.

Table 4.6: Plate A

n. elements	Method	n. sensors	RMS_u [%]	RMS_v [%]	RMS_w [%]
4x2	1	8	-	-	1.25
	2	8	-	-	1.33
	3	72	-	-	0.91
8x4	1	32	-	-	0.33
	2	32	-	-	0.29
	3	288	-	-	0.23
16x8	1	128	-	-	0.082
	2	128	-	-	0.081
	3	1152	-	-	0.056

Table 4.7: Plate B

n. elements	Method	n. sensors	RMS_u [%]	RMS_v [%]	RMS_w [%]
8x1	1	8	72.70	51.00	-
	2	8	72.70	51.00	-
	3	72	0.043	0.23	-
16x2	1	32	18.12	12.74	-
	2	32	0.11	0.080	-
	3	288	0.028	0.061	-
32x4	1	128	4.48	3.11	-
	2	128	0.098	0.061	-
	3	1152	0.020	0.026	-

Once the new approach is implemented, the models are analysed and the results shown in table 4.6 and 4.7 are obtained. For plate A, the results show a coherent yet not so remarkable decrease in error moving from methods 1 and 2 to method 3. Thus, the study would be more accurate but this precision might not be worth the expenses. To achieve similar results for the 4x2 plate, method 1 needs 8 sensors, while method 3 needs 72 of them.

On the contrary, plate B presents a significant error reduction when the third method is used. The results for 8x1 plate B are now accurate and the iFEM displacements are close to the direct FEM ones, whereas the ones obtained from method 1 and 2 are not acceptable due to great inaccuracy. In this case, the increase in the number of sensors is convenient: using method 3, the 8x1 plate (72 in-situ sensors) reaches a better accuracy

than the method 2 32x4 one (128 sensors). It can be concluded that, for in-plane loads, method 3 is both more accurate and cost-effective. However, it is possible to point out that the results obtained from method 2 with the 16x2 plate are also satisfactory: in this case, both errors are around 0.1%, and the sensors needed are less compared to the 72 sensors of the 8x1 plate. Thus, method 2 would be more cost-effective. The choice of both method and density of the inverse mesh is determined by different factors: if the purpose of the study is to reach greater accuracies (which would imply having the errors smaller than 0.1%) at the expense of raising the cost of tests, the analysis would be on a 8x1 plate using method 3, whereas if cost-effectiveness is needed the analysis would be on the 16x2 plate equipped with 32 sensors. Moreover, the computational costs must also be considered: the greater the number of inverse element, the longer it takes to run the inverse analysis. In case computing speed is required, the 8x1 plate studied with the third method is more suitable than the 16x2.

It is quite clear from the aforementioned examples that the usefulness of the third method can vary greatly depending on the load case. It is possible to have a major understanding of the reason why looking at both strain and sensor distributions for the two load cases. At the beginning, plate A presents a distribution of 4x2 elements, which implies the presence of two sensors in y-direction. Given the strain distributions, it is possible to notice that the deformations are well represented in both directions.  $\epsilon_x$  deformation, which is most accountable for the bending response, is perfectly described in its distribution by using this initial sensor location (the function is almost linear in both directions). The displacement is well approximated and the errors obtained are low, thus there is no need to overly increase the number of sensors by using method 3.

Plate B has originally a mesh of 8x1 elements, therefore for methods 1 and 2 the sensors are located at the centreline of the structure. In this case, the deformations are badly represented. The sensor locations prevent a good interpolation in width direction even in the case of linear trend. Moreover, the strains are more complex than in the previous case and the shear component  $\gamma_{xy}$  (which has no linear trend on the y-direction) must be taken into account. When two or more sensors are located in width direction the errors are subject to great decreases. It is now clear that method 3, having 3 sensors in y-direction, is able to provide a detailed solution also for the initial discretization.

In the following figures, the strain distributions are again reported. The red circles shown represent the strain components at the sensors location.

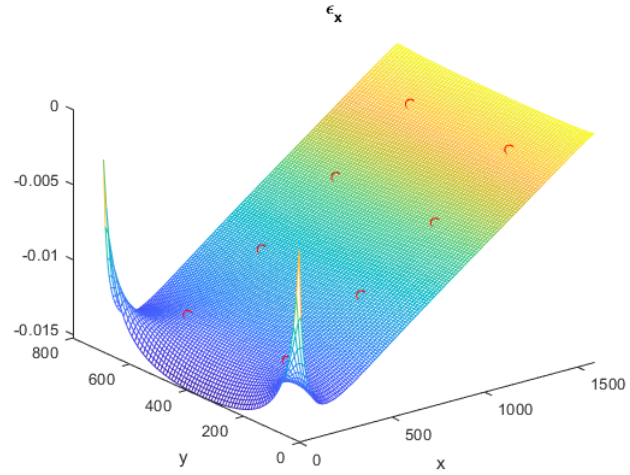


Figure 4.17: Plate A:  $\epsilon_x$  distribution and values at sensors location - 4x2 elements

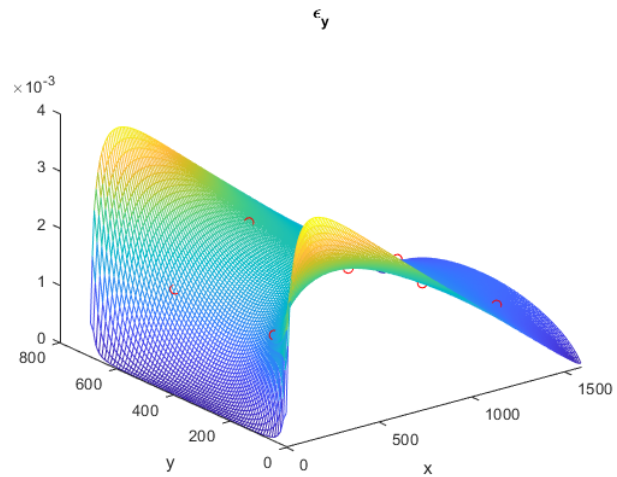


Figure 4.18: Plate A:  $\epsilon_y$  distribution and values at sensors location - 4x2 elements

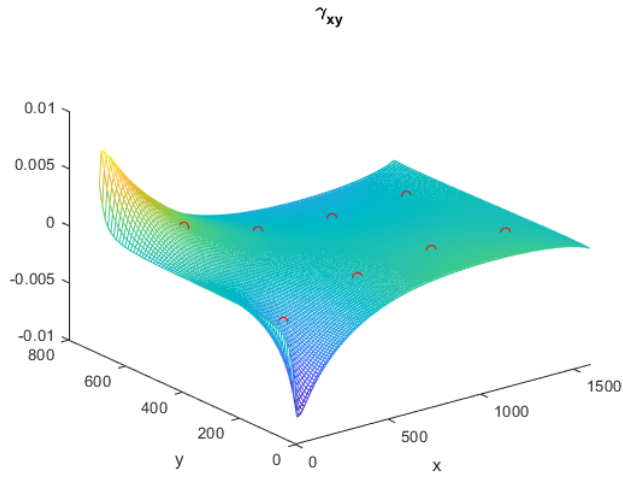


Figure 4.19: Plate A:  $\gamma_{xy}$  distribution and values at sensors location - 4x2 elements

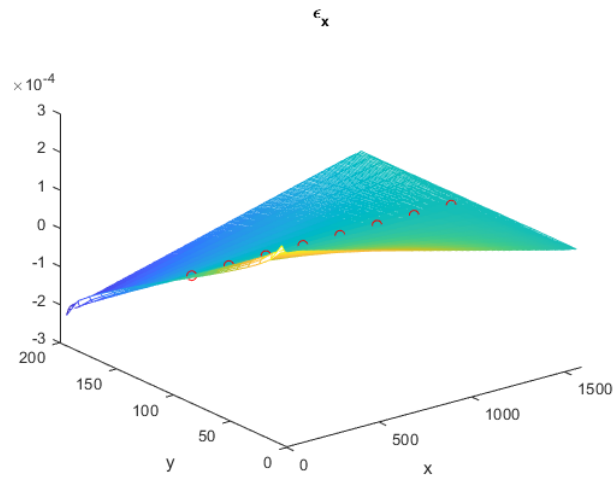


Figure 4.20: Plate B:  $\epsilon_x$  distribution and values at sensors location - 8x1 elements

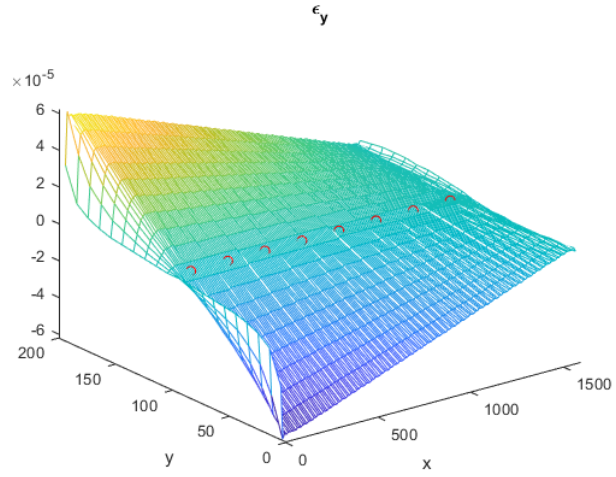


Figure 4.21: Plate B:  $\epsilon_y$  distribution and values at sensors location - 8x1 elements

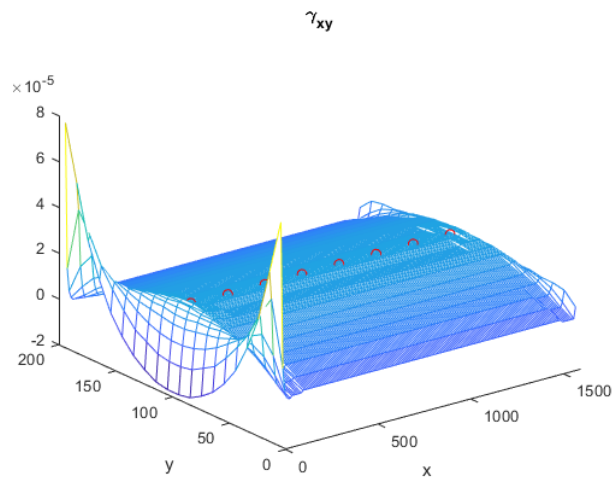


Figure 4.22: Plate B:  $\gamma_{xy}$  distribution and values at sensors location - 8x1 elements



## Chapter 5

# iFEM analysis of a spar

Once the efficiency of the different strain attribution methods has been evaluated over simple structures, it is possible to investigate the structural response obtained using the inverse finite element method over more complex systems. To this purpose, a cantilever spar is here considered. The structure has several non-negligible complications due to geometrical and material complexities which are examined in the following paragraphs. Nonetheless, this case presents several similarities to real structures commonly employed in aircraft; therefore, its study may provide deeper insight on the effectiveness of the iFEM method when applied to real life scenarios.

Considering the type of applied load, the most convenient method of strain attribution is consequently applied to each structural component, choosing from the procedures already introduced in chapter 3. This allows a more precise confrontation between the direct and indirect analyses. As in the previous chapter, the precision of the iFEM response is evaluated computing root mean square errors.

### 5.1 Geometry and properties

The structure is constituted by a web and two identical filleted flanges, which are located at the top and bottom of the web respectively. The main dimensions of the structures are reported in table 5.1.

Table 5.1: Dimensions

L	800 mm
h	362 mm
s	39.5 mm

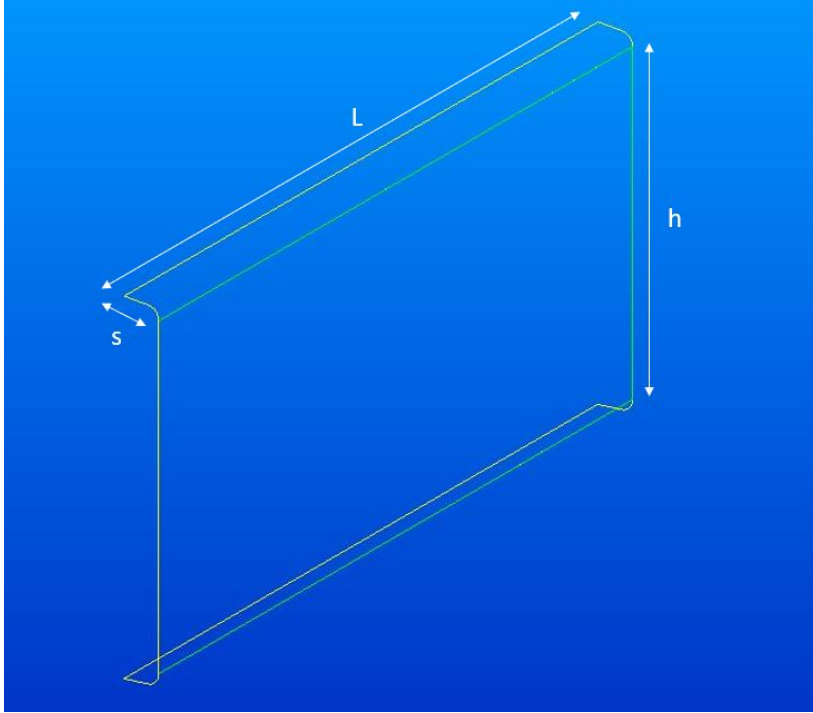


Figure 5.1: Geometry

The spar presents a complex geometry which has variable thickness: not only it varies between web and flanges, but it also decreases proceeding from the constraint to the free edge where the load is applied. Starting from the constraint, the laminate presents initially 26 plies of equal thickness differently oriented. At 244 mm from the constraint, the thickness of four of the central plies linearly decrease to zero. Therefore, the final section presents only 22 of the initial 26 plies. All the laminates are made of the same composite material, which has the following mechanical properties.

Table 5.2: Mechanical properties of the composite material

<b>Elastic Modulus (11)</b>	<b>Elastic modulus (22)</b>	<b>Poisson Ratio (12)</b>
127950 MPa	7730 MPa	0.3
<b>Shear modulus(12)</b>	<b>Shear modulus(23)</b>	<b>Shear modulus(13)</b>
3770 MPa	2520 MPa	3770 MPa

The coordinate system is defined as follows: the  $x$  axis is normal to the central part and directed towards the outside of the  $C$  shape, the  $y$  axis is directed along the span of the structure towards the constraint and the  $z$  axis is, accordingly, normal to the flanges. Both 26 and 24 plies materials are characterized by a symmetric fibre disposition with

Table 5.3: Half of the fiber disposition in both 26 and 22 plies material

<b>Fiber orientations: 26 plies materials</b>												
45°	-45°	0°	90°	0°	-45°	45°	0°	90°	-45°	45°	0°	90°
<b>Fiber orientations: 22 plies materials</b>												
45°	-45°	0°	0°	-45°	45°	90°	-45°	45°	0°	90°		

respect to the mid plane, which are oriented as shown in tables 5.3. The 0° orientation is parallel to the global y-direction.

The sequence of laminates and their properties is presented in tables 5.4 and 5.5. It is possible to notice that the materials are listed from the interlocking to the free edge and the section where thickness transition takes place is represented by the four material at the centre of both tables. The global length of the aforementioned thickness transition area is 25 mm.

Table 5.4: Web

<b>Laminate ID</b>	<b>Thickness</b>	<b>Number of plies</b>
20	4.99 mm	26
25	4.84 mm	26
26	4.68 mm	26
27	4.53 mm	26
28	4.38 mm	26
18	4.29 mm	22

Table 5.5: Flanges

Laminate ID	Thickness	Number of plies
19	5.30 mm	26
21	5.14 mm	26
22	4.98 mm	26
23	4.81 mm	26
24	4.65 mm	26
17	4.49 mm	22

The structure presents a quadrilateral mesh with varying dimension over the spar length. It is possible to notice that in the transition zone the mesh is refined with respect to the other parts, where element are slightly bigger. The mesh is also more accurate in the filleted areas. At the free edge of the spar holes are present, which are the cause of a band of non-quadrilateral elements. This section, even though present, does not undermine the accuracy of the results, since the deformation and stresses are zero there. The area is not taken into account since the load is here applied and the elements in the whole band are moving as one single part.

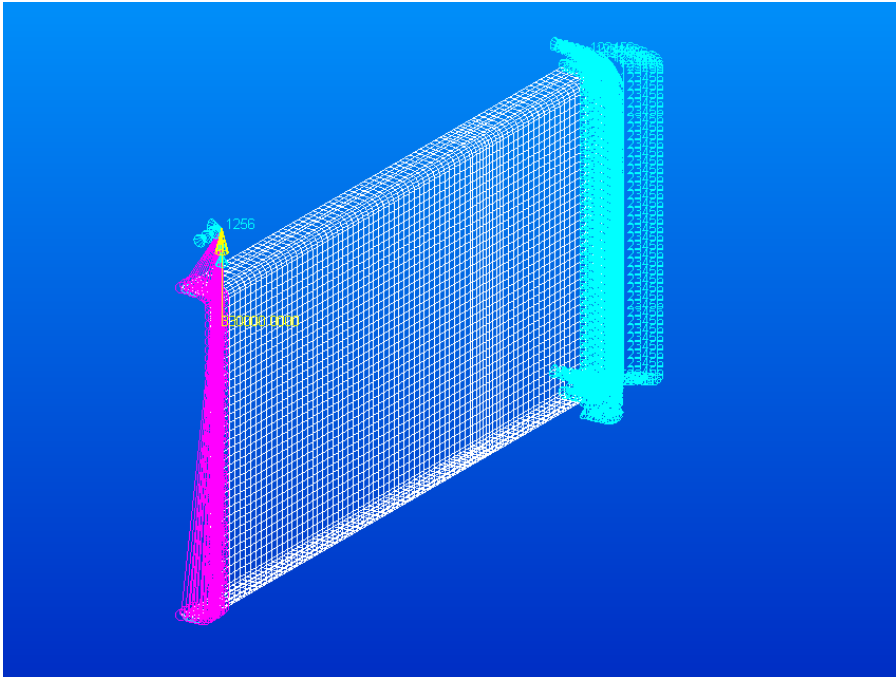


Figure 5.2: Spar discretisation

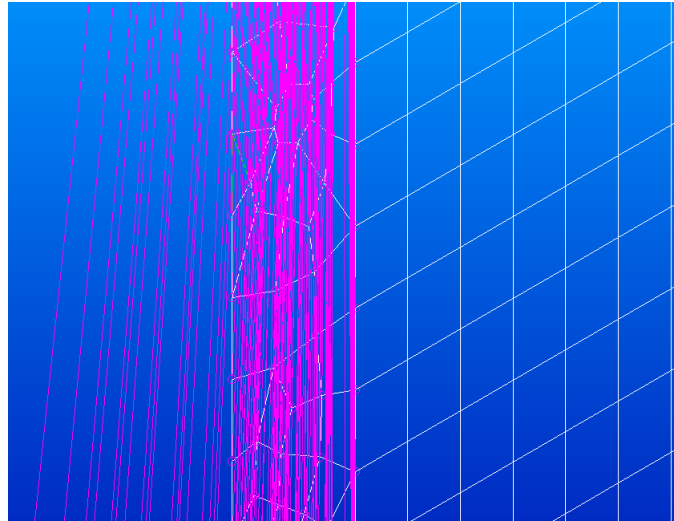


Figure 5.3: Details of the irregular mesh

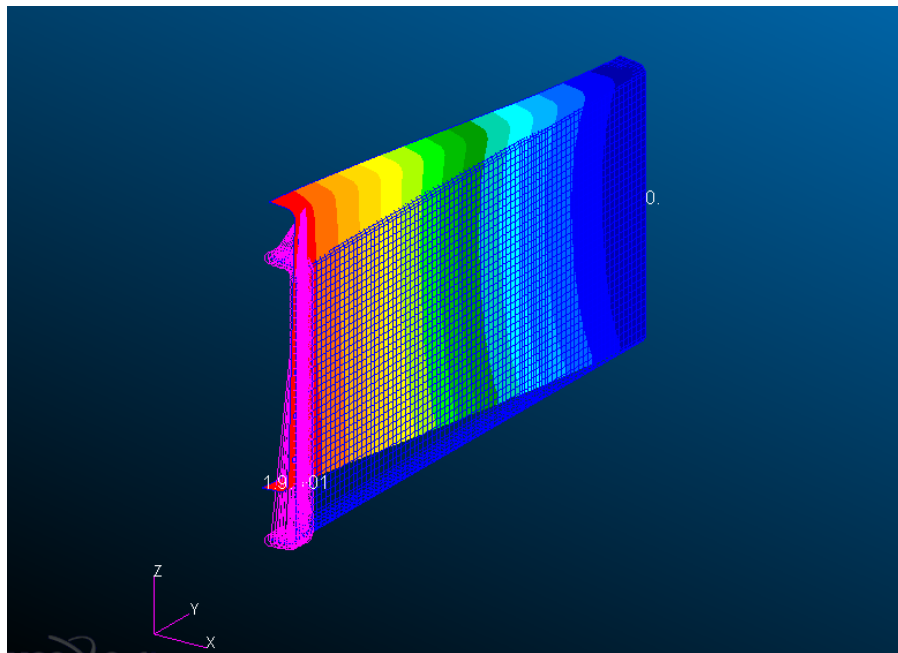


Figure 5.4: Structural response for direct FEM analysis

The structural response to a vertical load is shown in figure 5.4. The displacements obtained from this direct analysis will be later used as a benchmark for evaluating inverse FEM results. It should be noted that the complexity of this case is also due to its asymmetry, which causes a non trivial deformation across the structure. The iFEM accuracy will then depend heavily on that of the interpolation methods used to compute the strains, and on the choice of number and dimensions of the inverse elements.

## 5.2 Strain interpolation

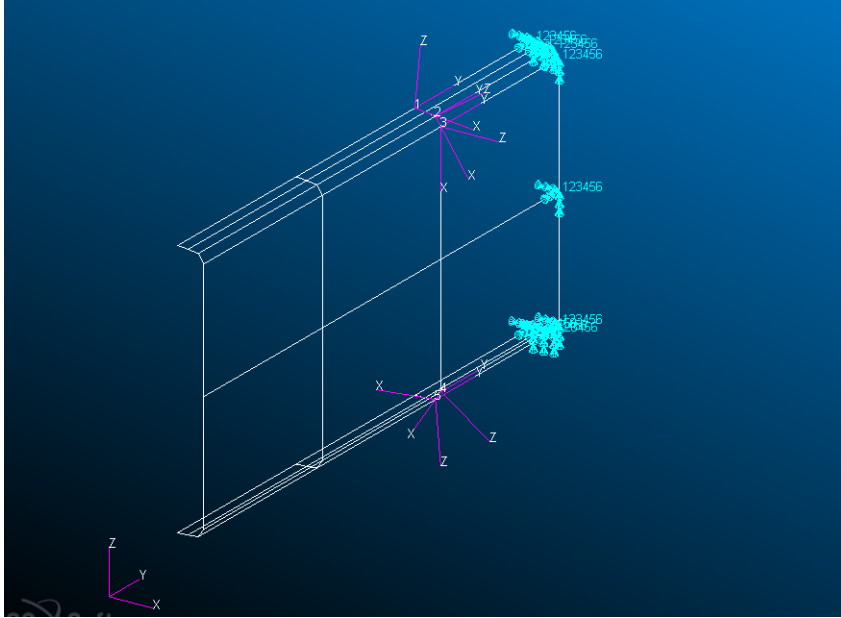


Figure 5.5: Inverse discretisation

The inverse discretization is hereby created. As the results obtained from the two plates analyses suggest, it is desirable to use different methods of strain attribution. The load is applied in parallel with z-direction, thus it is respectively normal to the flanges and parallel to the web. Therefore, it is assumed that the third method, where sensors are located at each Gauss point, is more suitable to study the web due to the type of applied load, whereas the second method is precise enough to describe the flanges behaviour. It is possible to notice in figure 5.5 that the inverse mesh is consequently less detailed over the web, over the flanges is instead denser.

As aforementioned, the strains used as input data for the inverse analysis are obtained from the interpolation of the ones found from the direct study. Some preliminary steps are to be carried out. First, strain data in the element centroids are obtained from the direct mesh using local reference systems, which are normal to the elements considered. Hence, the deformations are always referred to the local in-plane directions. This allows to always consider only three strain components, *i.e.*  $\varepsilon_x$ ,  $\varepsilon_y$  and  $\gamma_{xy}$ .

Because both of the complexity of the geometry, which results in strain data which may result difficult to properly interpolate across all of the structure, and of the organization of the elements inside the Patran-generated files, it was deemed unnecessary and counter-productive to try to perform a global interpolation, therefore opting for a local one. The



Table 5.6: initial RMS errors

RMS_u [%]	RMS_v [%]	RMS_w [%]
Inf	5.69	3.12

The results obtained for the  $v$  and  $w$  displacement components are already quite satisfactory, but a problem occurs in the computation of the  $u$  error. It is possible to notice from the Matlab results that in the direct analysis the  $u$  displacement is equal to zero at each node of the spar free edge, whereas it is different from zero in the results obtained from the inverse one as shown in figure 5.7. This is due to the presence in the direct model of a further constraint: the  $u$  displacement and the rotations about the  $y$  and  $z$  axes are bounded at each node of the spar tip.

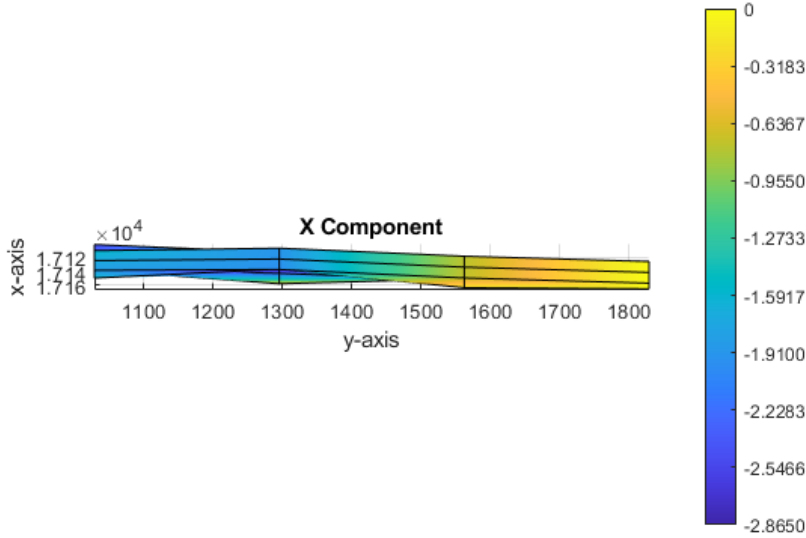


Figure 5.7: Spar displacement: x component

Once the results are evaluated, changes are made to the initial iFEM model. Firstly, the web nodes (and consequently also the ones on the flanges) are slightly moved in correspondence with nodes of the direct mesh, so that the error computation can be made over a larger number of nodes. Consequently, the error accuracy will be describing the structure global behaviour and not just the efficiency of the inverse method at the spar tip. The nodes in which displacements are evaluated are shown in figure 5.8. The boundary conditions at the spar free edge are also introduced in the inverse model, and the  $x$  component of displacement and the rotations about the  $y$  and  $z$  axes are bounded.

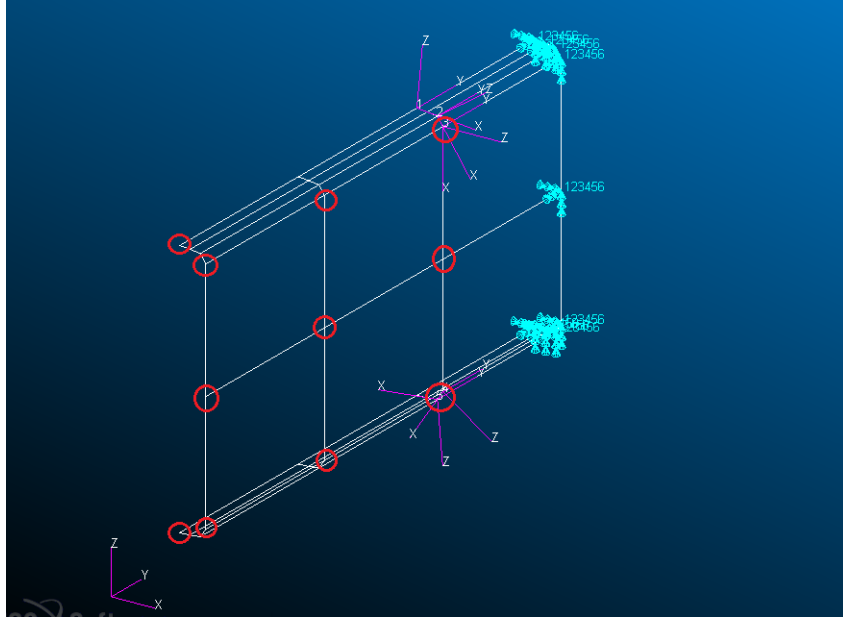


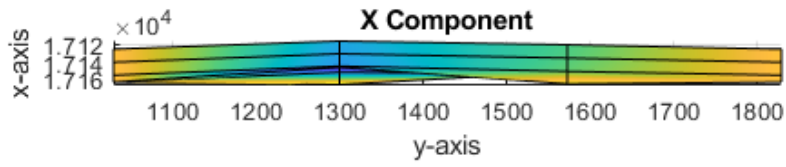
Figure 5.8: Nodes for errors computation

Table 5.7: RMS errors

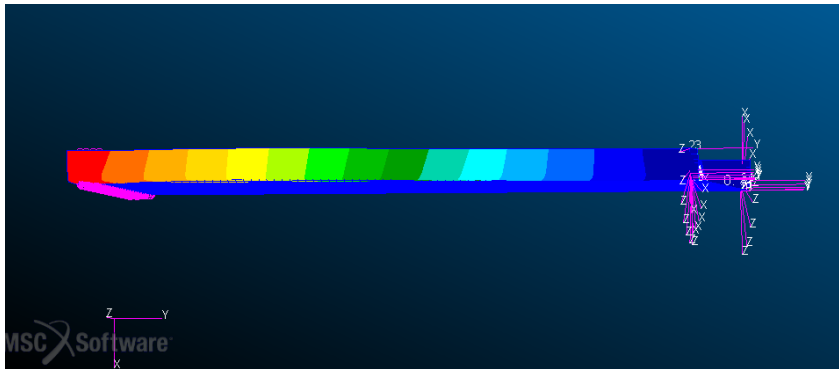
<b>RMS_u [%]</b>	<b>RMS_v [%]</b>	<b>RMS_w [%]</b>
39.06	3.10	2.35

It is possible to notice from table 5.7 that the RMS errors have globally decreased. The  $v$  and  $w$  errors, which were already quite satisfactory at the end of the first analysis, have improved of the 2% and 1% respectively. The  $u$  error has a finite value, but the error is still non-negligible. That could be due to the fact that the inverse mesh in the web area is too sparse, and so it cannot be precise in the depiction of transverse displacement even if the third method is used. In the previous chapter, the plate example with an in-plane loading did not show any error due to transverse displacements, and that could be caused by the different location of the loading and the simplicity of the structure. It was not possible to evaluate the effects of the methods on this displacement component.

Moreover, it is important to observe that displacements in the main directions,  $w$  and  $v$ , which represent the main structural responses to the load, are accurately described. The displacement in the normal direction to the web plane is smaller than the others, and as a consequence the presence of a major  $u$  error is less significant in terms of structural behaviour compared to the other two displacements. In figure 5.9 and 5.10 are shown the  $x$  component of the displacement obtained from both analyses and the global responses of the structure from both inverse and direct method.

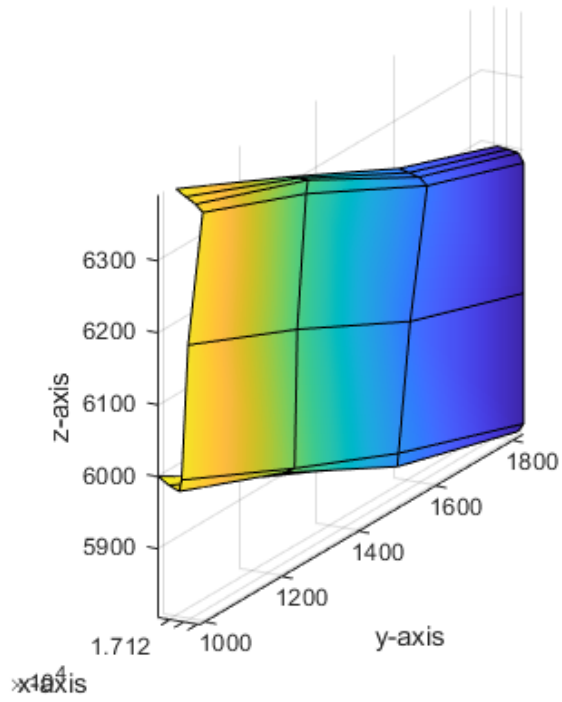


(a) *inverse FEM*

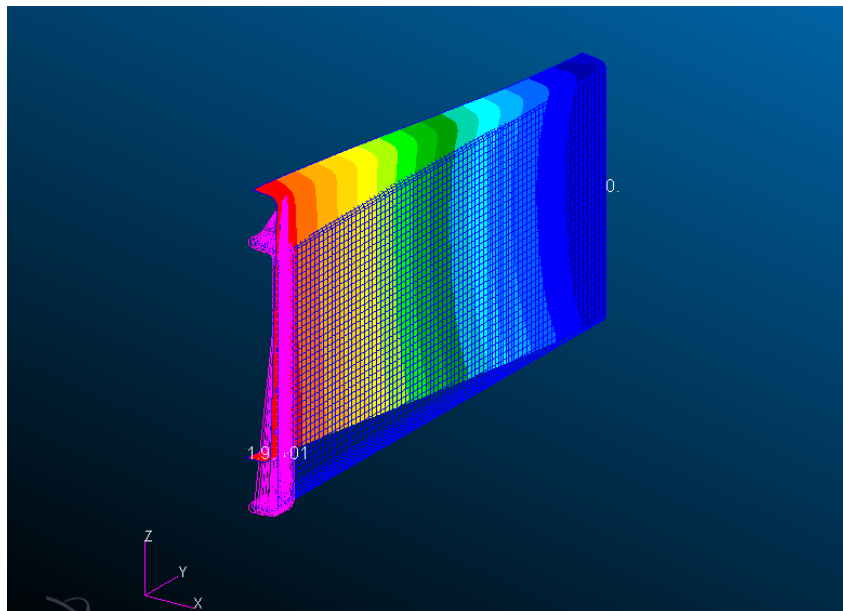


(b) *direct FEM*

Figure 5.9: Spar displacement: x component



(a) *inverse FEM*



(b) *direct FEM*

Figure 5.10: Spar response



## Chapter 6

# Conclusions

The main results will be hereafter summarized, with a focus on the central aspects emerging from the analyses that have been carried out. In this thesis, the potential of the inverse Finite Element Method has been investigated. The accuracy and applicability of the iFEM and of related procedures has been assessed using simplified cases derived from common aerospace structures. Moreover, different methods of strain attributions to each inverse element have been tested.

Firstly, the effectiveness of this variational approach is evaluated over two different aluminium plates, which present different geometries and are subject to different loadings. The validation of the inverse method analyses is focused primarily on the evaluation of three different approaches for the attribution of strain input values to the Gauss points of each inverse element. Two initial sparse meshes are created to compare methods 1 and 2. It is found that the errors are already quite satisfactory for the plate subject to out-of-plane loading, whereas the program was not able to depict the structural behaviour of the plate subject to in-plane loading. The analysis of both plates is then carried out for denser meshes and the results coherently improve. When compared to the results obtained from the third method, which attributes the exact strain data to the nine Gauss points using nine different sensors at each location, several considerations can be made. For the plate subjected to out-of-plane loading, the results show a coherent yet not so remarkable decrease in error moving from methods 1 and 2 to method 3. Consequently, by using exact strain data at each Gauss point location, the analysis is more accurate but this precision might not be worth the expenses in terms of the substantial increase of sensors. On the contrary, the plate subjected to in-plane loading presents a significant error reduction when the third method is used. The iFEM displacements are close to the direct FEM ones even using the sparser mesh, whereas the ones obtained from method 1 and 2 are not acceptable due to great inaccuracy. Nevertheless, it is possible to notice

that the results obtained from denser meshes are satisfactory also in case method 2 is used. It is then clear that the choice of the mesh density and of the strain attribution method (and consequently the choice of the number of sensor for each element) are based on the purpose of the analysis. If cost-effectiveness is desired, the most suitable choice would be to have a denser mesh with sensors located at the centroids of the inverse elements, at the expenses of computing speed, which is inversely proportional to the number of inverse elements employed. On the contrary, if greater accuracies and computing speed are requested, a sparser mesh with nine sensors over each element should be chosen.

Subsequently, the structural response of a more complex system obtained using the inverse finite element method has been investigated. In this case, a numerical study of an existing spar structure is carried out. The results obtained from the previous study are applied, and it is possible to use different methods of strain attribution for each part of the structure. The analysis is then carried out and the resultant errors are computed. For what concerns the component  $v$  and  $w$  of the structural displacement, the errors obtained from the analysis are satisfactory, whereas it is possible to notice that the error in  $u$  component could not properly describe the real spar displacement. That could be caused by the sparsity of the inverse discretization in the web area, and so it cannot be accurate in the depiction of transverse displacement even if the third method is used. Moreover, the former plate study subjected to an in-plane load considered pure shear, no combined effect on the displacement was taken into account, thus it was not possible to evaluate in this sense any of the methods applied. It is mostly important to notice that the displacements in the main directions,  $w$  and  $v$ , which represent the main structural responses to the load, are properly depicted. The displacement in the normal direction to the web plane is smaller than the other components, and as a consequence the presence of a major error in this direction is less significant in terms of structural behaviour with respect to the other two displacement errors.

## Future developments

Starting from the present work, some additional research might be carried out to further broaden the subject. The possible developments are:

- The determination of the optimal number of sensors and of their placement over the structure. It may also be worth investigating if certain placement patterns lead to a reduction in the number of sensors needed. Still, this is a task heavily affected by the actual shape of the examined structure, so it may be solved accurately only for simple cases such as beams and plates;

- The implementation of a program which is able to streamline the deformation reconstruction process and make it suitable to describe more complex geometries;
- Since the work has been focusing on numerical studies of existing structures, experimental tests with actual in-situ sensors could be performed;
- Tests on different structures subject to combined loads, to verify their effects on the lesser component of displacement;
- As a consequence of the previous point, the study of more complex geometries with the inverse method would be desirable, choosing the most suitable method of strain attribution (and consequently the number of sensors employed for each element). As done in this study, the obtained results would be compared with the ones obtained from a direct FEM analysis.



# Bibliography

- [1] W Akl, S Poh, and A Baz. “Wireless and distributed sensing of the shape of morphing structures”. In: *Sensors and Actuators A: Physical* 140.1 (2007), pp. 94–102.
- [2] Brandon Arritt et al. “Demonstration of the Use of Fiber-Optics, with Integrated Fiber-Bragg Gratings, for Shape Determination of Large Deployable Structures”. In: *48th AIAA/ASME/ASCE/AHS/ASC Structures, Structural Dynamics, and Materials Conference*. 2007, p. 2006.
- [3] R Bruno, N Toomarian, and M Salama. “Shape estimation from incomplete measurements: a neural-net approach”. In: *Smart Materials and Structures* 3.2 (1994), p. 92.
- [4] Marco Gherlone, Priscilla Cerracchio, and Massimiliano Mattone. “Shape sensing methods: Review and experimental comparison on a wing-shaped plate”. In: *Progress in Aerospace Sciences* 99 (2018), pp. 14–26.
- [5] Marco Gherlone et al. “Shape sensing of 3D frame structures using an inverse finite element method”. In: *International Journal of Solids and Structures* 49.22 (2012), pp. 3100–3112.
- [6] R Glaser, V Caccese, and M Shahinpoor. “Shape monitoring of a beam structure from measured strain or curvature”. In: *Experimental mechanics* 52.6 (2012), pp. 591–606.
- [7] Murali Gopinathan et al. “Recursive estimation of displacement and velocity in a cantilever beam using a measured set of distributed strain data”. In: *Journal of intelligent material systems and structures* 6.4 (1995), pp. 537–549.
- [8] Mark Hopkins et al. “Smart skin conformal load-bearing antenna and other smart structures developments”. In: *38th Structures, Structural Dynamics, and Materials Conference*. 1997, p. 1163.
- [9] Adnan Kefal et al. “A quadrilateral inverse-shell element with drilling degrees of freedom for shape sensing and structural health monitoring”. In: *Engineering science and technology, an international journal* 19.3 (2016), pp. 1299–1313.

- [10] George C Kirby III et al. “Strain-based shape estimation algorithms for a cantilever beam”. In: *Smart Structures and Materials 1997: Smart Structures and Integrated Systems*. Vol. 3041. International Society for Optics and Photonics. 1997, pp. 788–798.
- [11] William L Ko, W Lance Richards, and Van Tran Fleischer. “Applications of Ko displacement theory to the deformed shape predictions of the doubly-tapered Ikhana Wing”. In: (2009).
- [12] Zhu Mao and Michael Todd. “Comparison of shape reconstruction strategies in a complex flexible structure”. In: *Sensors and Smart Structures Technologies for Civil, Mechanical, and Aerospace Systems 2008*. Vol. 6932. International Society for Optics and Photonics. 2008, 69320H.
- [13] Alexander Tessler and Jan L Spangler. “A least-squares variational method for full-field reconstruction of elastic deformations in shear-deformable plates and shells”. In: *Computer methods in applied mechanics and engineering* 194.2-5 (2005), pp. 327–339.
- [14] Alexander Tessler and Jan L Spangler. “A variational principle for reconstruction of elastic deformations in shear deformable plates and shells”. In: (2003).
- [15] Alexander Tessler and Jan L Spangler. “Inverse FEM for full-field reconstruction of elastic deformations in shear deformable plates and shells”. In: (2004).
- [16] Alexander Tessler et al. “Shape Sensing of Plate and Shell Structures Undergoing Large Displacements Using the Inverse Finite Element Method”. In: *Shock and Vibration* 2018 (2018).
- [17] Peter Wriggers. “Computational contact mechanics”. In: *Computational Mechanics* 32.1-2 (2003), pp. 141–141.
- [18] Weilong Yin et al. “Structural shape sensing for variable camber wing using FBG sensors”. In: *Sensors and Smart Structures Technologies for Civil, Mechanical, and Aerospace Systems 2009*. Vol. 7292. International Society for Optics and Photonics. 2009, 72921H.